ATLAS CONF Note

ATLAS-CONF-2017-080

December 14, 2017

Search for photonic signatures of gauge-mediated supersymmetry in 13 TeV pp collisions with the ATLAS detector

The ATLAS Collaboration

A search is presented for photonic signatures motivated by generalized models of gauge-mediated supersymmetry breaking. This search makes use of 36.1 fb^{-1} of proton–proton collision data at $\sqrt{s}$ = 13 TeV recorded by the ATLAS detector at the LHC, and explores models dominated by both strong and electroweak production of supersymmetric partner states. Experimental signatures incorporating an isolated photon and significant missing transverse momentum are explored. These signatures include events with an additional photon or additional jet activity not associated with any specific underlying quark flavor. No significant excess of events is observed above the Standard Model prediction and 95% confidence-level upper limits of between 0.083 and 0.32 fb are set on the visible cross section of contributions from physics beyond the Standard Model. These results are interpreted in terms of lower limits on the masses of gluinos, squarks, and gauginos in the context of generalized models of gauge-mediated supersymmetry, which reach as high as 2.3 TeV for strongly-produced and 1.3 TeV for weakly-produced supersymmetric partner pairs.

ATLAS-CONF-2017-080
14 December 2017

Contents

1 Introduction

This paper reports on a search for two complementary classes of events containing energetic isolated photons and large missing transverse momentum (with magnitude denoted $E_{\mathrm{T}}^{\mathrm{miss}}$). The search is performed with proton–proton (pp) collision data at a center-of-mass energy $\sqrt{s} = 13$ TeV corresponding to an integrated luminosity of 36.1 fb^{-1} recorded with the ATLAS detector at the Large Hadron Collider (LHC) in 2015 and 2016. For the first of the two classes, two isolated energetic photons are required ("diphoton" events), while for the second class only a single isolated photon is required, in combination with multiple hadronic jets ("photon+jets" events).

The results of searches for these two classes of events are used to derive model-independent limits on potential contributions from as-of-yet undiscovered physical processes. The results are also interpreted in the context of several general models of gauge-mediated supersymmetry breaking (GGM) [1, 2]. These models include both the production of supersymmetric partners of strongly coupled Standard Model (SM) particles as well as the production of partners of SM particles possessing only electroweak charge. In all models of GGM, the lightest supersymmetric particle (LSP) is the gravitino $\tilde{G}$ (the partner of the hypothetical quantum of the gravitational field), with a mass significantly less than 1 GeV. In the GGM models considered here, the decay of the supersymmetric states produced in LHC collisions would proceed through the next-to-lightest supersymmetric particle (NLSP), which would then decay to the $\tilde{G}$ LSP and one or more SM particles. Each of the two event classes corresponds to a specific choice of NLSP, each of which in turn has a high probability of decay into $\gamma + \tilde{G}$. In all models considered, all supersymmetric states with the exception of the $\tilde{G}$ are short lived, leading to prompt production of SM particles that are observed in the ATLAS detector. The result based on the diphoton signature extends and supplants an ATLAS search [3] performed with an integrated luminosity of 3.2 fb^{-1} of pp collision

data taken at a center-of-mass energy of $\sqrt{s} = 13\,\text{TeV}$, and complements searches [4, 5] performed by the CMS Collaboration making use of $35.9\,\text{fb}^{-1}$ of $\sqrt{s} = 13\,\text{TeV}$ pp collision data. The result based on the photon+jets signature extends and supplants an ATLAS search [6] performed with an integrated luminosity of $20.3\,\text{fb}^{-1}$ of 8 TeV pp collision data.

The paper is organized as follows. More detail on the theoretical background is provided in the Section 2. Section 3 presents the salient features of the ATLAS detector. Section 4 provides details of the Monte Carlo simulations used in the analysis for background and signal processes. Section 5 discusses the reconstruction and identification of photons, leptons, jets, and whole-event observables relevant to the event selection, while Section 6 describes the event selection itself. The estimation of background contributions and signal efficiency, and the study of systematic uncertainties are discussed in Sections 7 and 8. The results are presented in Section 9 and are interpreted in terms of limits on various GGM models. Finally, Section 10 is devoted to the conclusions.

2 Gauge-mediated supersymmetry phenomenology

Supersymmetry (SUSY) [7–14] introduces a symmetry between fermions and bosons, resulting in a SUSY partner (sparticle) for each SM particle with identical quantum numbers except a difference by half a unit of spin. As none of these sparticles have been observed, SUSY must be a broken symmetry if realized in nature. Assuming R-parity conservation [15–19], sparticles are produced in pairs. These then decay through cascades involving other sparticles until the stable, weakly interacting LSP is produced, leading to a final state with significant $E_{\text{T}}^{\text{miss}}$.

This paper considers experimental signatures directed towards models inspired by gauge-mediated SUSY breaking [20–25]. These signatures are largely determined by the nature of the NLSP; in GGM models, the NLSP is often formed from an admixture of any of the SUSY partners of the electroweak gauge and Higgs bosons. In this study, two cases are considered for the composition of the NLSP, both of which would produce photonic signatures in the ATLAS detector. In the first case, the NLSP is assumed to be purely bino-like (the SUSY partner of the SM $U(1)$ gauge boson), while in the second case, the NLSP is assumed to be an admixture of bino and neutral higgsino states. In this paper, the neutral NLSP is denoted $\tilde{\chi}_1^0$ irrespective of its composition.

Where not explicitly constrained by the assumptions of the specific GGM models under study, the masses and properties of SUSY partner states are controlled by several underlying parameters. These include the $U(1)$, $SU(2)$ and $SU(3)$ gauge partner mass parameters (M_1, M_2 and M_3, respectively), the higgsino mass parameter μ, the gravitino mass, and the ratio $\tan\beta$ of the two SUSY Higgs-doublet vacuum expectation values. A value of 1.5 is chosen for the latter; for all GGM models considered, the phenomenology relevant to this search is only weakly dependent on the value of $\tan\beta$.

In the case that the NLSP is bino-like, the final decay in each of the two cascades in a GGM SUSY event is predominantly $\tilde{\chi}_1^0 \to \gamma + \tilde{G}$, leading to final states with two photons and missing transverse momentum. In the case that the NLSP is a mixture of the bino and higgsino, the higgsino mass parameter μ is chosen to be positive, leading to final decays split primarily between the modes $\tilde{\chi}_1^0 \to \gamma + \tilde{G}$ and $\tilde{\chi}_1^0 \to Z + \tilde{G}$, and thus a preponderance of final states with a single photon accompanied by multiple jets and $E_{\text{T}}^{\text{miss}}$. To provide a signature advantageous for the photon+jets analysis, the values of μ and M_1 are chosen so that, to within $\sim 1\%$, the $\tilde{\chi}_1^0$ branching ratios are $\text{B}(\tilde{\chi}_1^0 \to \gamma\tilde{G}) \sim 50\%$, $\text{B}(\tilde{\chi}_1^0 \to Z\tilde{G}) \sim 49\%$ and $\text{B}(\tilde{\chi}_1^0 \to h\tilde{G}) \sim 1\%$, irrespective of the mass of the $\tilde{\chi}_1^0$ (h represents the scalar state observed at 125 GeV, assumed here

to be the lightest CP-even state of the SUSY Higgs spectrum). Although not explored here, the choice $\mu < 0$ would lead to decays that prefer the production of the h boson over the Z boson, producing decays rich in b-quark jets but otherwise similar to the $\mu > 0$ case.

The results of the diphoton and photon+jets analyses are interpreted in the context of four distinct GGM models. Three of the GGM models are associated with the diphoton analysis, each featuring a purely bino-like NLSP and distinguished by the state directly produced by the proton–proton collision. For the first of the three GGM models associated with the diphoton analysis, referred to as the "gluino–bino" model, production proceeds through a degenerate octet of gluinos, collectively denoted as $\tilde{g}$ (Figure 1 left). For the second of these models (the "wino–bino" model; Figure 1 right), production proceeds through a degenerate triplet of the $SU(2)$ gauge partner (wino, or $\tilde{W}$) states $\tilde{\chi}_2^0$ and $\tilde{\chi}_1^\pm$, and is dominated by the production of $\tilde{\chi}_1^+\ \tilde{\chi}_1^-$ and $\tilde{\chi}_2^0\ \tilde{\chi}_1^\pm$. For the third of these models (the "squark–bino" model; Figure 2 left), production proceeds through the squark states.[1] All squark states are taken to be degenerate in mass, with the exception of the partners of the three right-handed up-type quarks, whose masses are decoupled (set to inaccessibly large values) in order to satisfy GGM sum rules [2]. For a bino-like NLSP, the cross section for direct $\tilde{\chi}_1^0$ pair production is essentially zero for any value of the $\tilde{\chi}_1^0$ mass. For the "higgsino–bino" GGM model associated with the photon+jets analysis (Figure 2 right), for which the NLSP is chosen to be a mixture of the bino and higgsino, production again proceeds through a degenerate octet of gluino states. In this last case, however, there is a leading-order coupling between initial-state partons and the higgsino component of the $\tilde{\chi}_1^0$, leading to a SUSY production process dominated by $\tilde{\chi}_1^0$ pair production for low values of the $\tilde{\chi}_1^0$ mass. However, the efficiency for detecting such events in the photon+jets analysis is very small, and so direct $\tilde{\chi}_1^0$ pair production is expected to play no role in the analysis.

For all four GGM models, the masses of both the NLSP and the directly produced states are taken to be free parameters of the model, with all other SUSY partner masses other than those of the gravitino and h state decoupled. The lifetime $\tau_{\tilde{\chi}_1^0}$ of the NLSP is set so that $c\tau_{\tilde{\chi}_1^0}$ is never greater than 0.1 mm. This ensures that all particles arising from the decay of the NLSP are prompt, and in particular that the relationship between the direction and the point of impact on the face of the calorimeter of photons from NLSP decay is consistent with that of a prompt photon (a separate analysis [26] searches for GGM models with a longer-lived bino-like NLSP, leading to signatures with non-prompt photons).

3 ATLAS detector

The ATLAS detector [27] consists of an inner tracking system surrounded by a superconducting solenoid, electromagnetic (EM) and hadronic sampling calorimeters, and a muon spectrometer. The inner detector is immersed in a 2 T axial magnetic field, and consists of pixel and silicon microstrip (SCT) detectors inside a transition radiation tracker, providing charged-particle tracking in the region $|\eta| < 2.5$.[2] For the $\sqrt{s} = 13$ TeV run, a fourth layer of the pixel detector, the "insertable B-Layer" [28], was inserted at an average radius

[1] For the case of left-handed top squark (stop) production when $m_{\text{stop}} < m_{\tilde{\chi}_1^0} + m_{\text{top}}$, the stop decay proceeds through an effective neutral current interaction to a charm or up quark accompanied by the bino-like $\tilde{\chi}_1^0$.

[2] ATLAS uses a right-handed coordinate system with its origin at the nominal interaction point (IP) in the center of the detector and the z axis along the beam pipe. The x axis points from the IP to the center of the LHC ring, and the y axis points upwards. Cylindrical coordinates (r, ϕ) are used in the transverse plane, ϕ being the azimuthal angle measured relative to the x axis. The pseudorapidity is defined in terms of the polar angle θ as $\eta = -\ln[\tan(\theta/2)]$. Angular distance is measured in units of $\Delta R \equiv \sqrt{(\Delta\eta)^2 + (\Delta\phi)^2}$. A related quantity, ΔR_y, makes use of rapidity y rather than pseudorapidity η to define phase-space separation: $\Delta R_y \equiv \sqrt{(\Delta y)^2 + (\Delta\phi)^2}$.

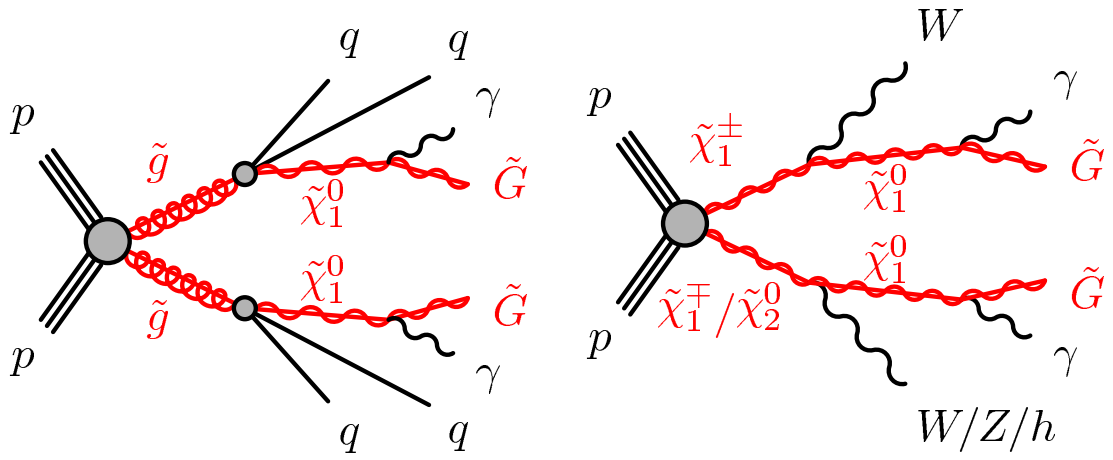

Figure 1: Typical production and decay processes for the (left) gluino-production and (right) electroweak-production instances of the GGM model for which the NLSP is a bino-like neutralino. These models are referred to in the text as the gluino–bino and wino–bino models, respectively.

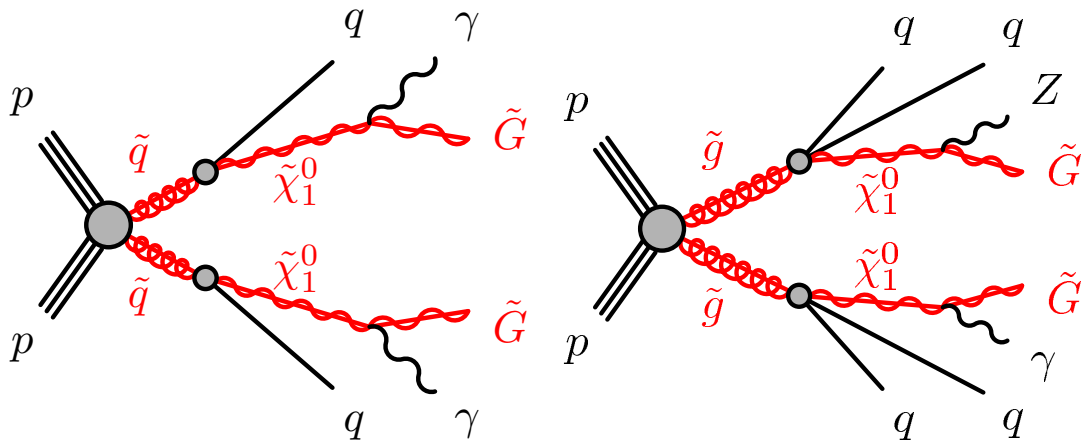

Figure 2: Typical production and decay processes for (left) the squark-production instance of the GGM model for which the NLSP is a bino-like neutralino, and (right) the gluino-production instance of the GGM model for which the NLSP is a higgsino–bino neutralino admixture. These models are referred to in the text as the squark–bino and higgsino–bino models, respectively.

of 33.2 mm. The EM calorimeter uses lead as the absorber and liquid argon (LAr) as the active material. In the central rapidity region $|\eta| \lessapprox 1.5$, the EM calorimeter is divided into three longitudinal layers, one of them segmented in highly granular η strips for optimal γ/π^0 separation. The EM calorimeter is augmented by a presampler layer for $|\eta| < 1.8$. Hadron calorimetry is based on different detector technologies, with scintillator tiles ($|\eta| < 1.7$) or LAr ($1.5 < |\eta| < 4.9$) as the active medium, and with steel, copper, or tungsten as the absorber material. The muon spectrometer consists of superconducting air-core toroids, a system of trigger chambers covering the range $|\eta| < 2.4$, and high-precision tracking chambers allowing muon momentum measurements for $|\eta| < 2.7$. ATLAS uses a two-level trigger system to select events [29]. A low-level hardware trigger is implemented in custom electronics and reduces the data rate to a

design value of ~ 100 kHz using a subset of detector information. A high-level software trigger selects events with interesting final states using software algorithms that access the full detector information, reducing the average accepted event rate to ~ 1 kHz.

4 Samples of simulated processes

Simulated samples of various pp collision processes are used to estimate the signal efficiency, develop and optimize the signal region (SR) selection, and in some cases estimate SM background contributions to the SRs. For the GGM model used to interpret the photon+jets results, the SUSY mass spectra and branching ratios are calculated using SUSPECT 2.43 [30] and SDECAY 1.5 [31], respectively, inside the package SUSY-HIT 1.5a [32], and with Higgs boson decay provided by HDECAY 3.4 [33]. For the GGM models used to interpret the diphoton results, the SUSY mass spectra and branching ratios are calculated using SUSPECT 2.41 [30] and SDECAY 1.3b [34], respectively. For all models, the Monte Carlo (MC) SUSY signal samples were generated to leading-order accuracy using MG5_aMC@NLO v2.3.3 [35], with up to two extra partons included beyond the underlying $2 \to 2$ SUSY production process. The simulation used the NNPDF2.3LO parton distribution functions (PDF) set [36], and was interfaced to PYTHIA 8.212 [37] with the ATLAS A14 set of tuned parameters [38] for the modeling of the parton showering (PS), hadronization and underlying event. Strong and electroweak SUSY production cross sections are calculated to next-to-leading order (NLO) in the strong coupling constant, adding the resummation of soft gluon emission at next-to-leading-logarithmic accuracy (NLO+NLL) [39–45]. The nominal cross section and the uncertainty are taken from an envelope of cross-section predictions using different PDF sets and factorization and renormalization scales, as described in Ref. [46].

While most of the backgrounds to the GGM models under examination are estimated through the use of control samples selected from data, as described below, the extrapolation from control regions (CRs) to signal regions depends on simulated samples, as do the optimization studies. Simulated SM processes include single-photon and diphoton production both with and without an associated vector boson, $t\bar{t}$ production both with and without an accompanying photon, and multijet production. With the exception of the $t\bar{t}\gamma$ process, Standard Model processes were generated using the SHERPA v2.1.1 simulation package [47], making use of the CT10 [48] PDF set. Matrix elements are calculated for up to three-parton emission at leading order (LO) using the COMIX [49] generator and then combined with the SHERPA parton shower [50] according to an improved CKKW procedure [51]. The $t\bar{t}\gamma$ process was generated to next-to-leading order accuracy using MG5_aMC@NLO v2.3.3 [35] in conjunction with PYTHIA 8.186 [52] with the NNPDF2.3LO PDF set [36] and the A14 set of tuned parameters [38].

All MC samples were processed with the GEANT4-based simulation [53, 54] of the ATLAS detector, or, where appropriate, a simulation of the ATLAS detector based on parametrized shower shapes in the calorimeter, and GEANT4 elsewhere. Corrections are applied to the simulated samples to account for differences between data and simulation in the photon-based trigger, identification, and reconstruction efficiencies, as well as for the efficiency and misidentification rate of the algorithm used to identify jets containing b-hadrons (b-tagging). The variation in the number of pp interactions per bunch crossing ("pileup") as a function of the instantaneous luminosity is taken into account by overlaying simulated minimum-bias events according to the observed distribution of the number of pileup interactions in data, with an average of 23.7 interactions per event.

5 Reconstruction of candidates and observables

Primary vertices are formed from sets of two or more tracks, each with transverse momentum $p_{\mathrm{T}} > 400\,\mathrm{MeV}$, that are consistent with having originated at the same three-dimensional space point within the luminous region of the colliding proton beams. When more than one such primary vertex is found, the vertex with the largest scalar sum of the squared transverse momenta of the associated tracks is chosen.

Electron candidates are reconstructed from EM calorimeter energy clusters consistent with having arisen from the impact of an electromagnetic particle (electron or photon) upon the face of the calorimeter. For the object to be considered an electron, it is required to match a track reconstructed by an algorithm optimized for recognizing charged particles with a high probability of bremsstrahlung. Electrons are required to pass a "tight" set of identification requirements as defined in Refs. [55–57], based on the characteristics of the EM shower development, the quality of the associated reconstructed track, and the quality of the association of the track with the calorimeter deposition. Electron candidates used by these searches are further required to have $p_{\mathrm{T}} > 25\,\mathrm{GeV}$ and $|\eta| < 2.47$, but excluding the transition region $1.37 < |\eta| < 1.52$ between the barrel and end-cap calorimeters. A track-based isolation requirement is imposed, with the scalar sum of the transverse momenta of tracks within a cone of size $\Delta R = 0.2$ (excluding that of the electron candidate's track) required to be less than a value that leads to a loss of efficiency of 5% for electrons with $p_{\mathrm{T}} = 25$ GeV, and of less than 1% for electrons with $p_{\mathrm{T}} > 60$ GeV. Finally, the electron track is required to be consistent with having originated from the primary vertex in the r–z plane.

Electromagnetic clusters in the range $|\eta| < 2.37$ (excluding the transition region $1.37 < |\eta| < 1.52$) are classified as photon candidates provided that they either have no matched track ("unconverted" photons) or have one or more matched tracks consistent with having originated from a photon conversion vertex ("converted" photons). Photon candidates are required to have $E_{\mathrm{T}}^{\gamma} > 25$ GeV, where E_{T}^{γ} is the energy of the photon candidate, measured in the EM calorimeter, multiplied by the cosine of the angle of its trajectory relative to the plane perpendicular to the z axis. Photons candidates are also required to fulfill "loose" or "tight" identification criteria [58, 59] based on observables that reflect the shape of the electromagnetic showers in the calorimeter, in particular in the finely segmented first layer. While tight photons are required for all SRs, loose photons are used to construct control samples that aid in the estimation of backgrounds arising from mis-reconstructed jets. The photon direction is estimated either using EM calorimeter longitudinal segmentation (if unconverted) or the position of the conversion vertex (if converted), together with constraints from the pp collision point. In the case that an EM calorimeter deposition is identified as both a photon and an electron, the photon candidate is discarded and the electron candidate retained. Additionally, a calorimeter-based isolation requirement is imposed: after correcting for contributions from pileup and the deposition ascribed to the photon itself, the transverse energy $E_{\mathrm{T}}^{0.4}$ deposited in a cone of size $\Delta R = 0.4$ surrounding the photon candidate's energy deposition must satisfy the relation $E_{\mathrm{T}}^{0.4} < 2.75\,\mathrm{GeV} + 0.22 \times E_{\mathrm{T}}^{\gamma}$, with E_{T}^{γ} in GeV.

Muon candidates are reconstructed via a combination of track information from the muon spectrometer and the inner tracking systems. Muons must pass the "medium" identification requirements defined in Ref. [60], based on requirements on the number of hits in the different inner detector and muon spectrometer subsystems, and on the significance of the charge-to-momentum ratio measurement. Muon candidates are required to have $p_{\mathrm{T}} > 25\,\mathrm{GeV}$ and $|\eta| < 2.7$. Muon candidates are also required to pass an isolation requirement identical to that for electron candidates. Finally, the muon track is required to be consistent with having originated from the primary vertex in both the r–z and r–ϕ planes.

Making use of utilities within the FastJet package [61], jets are reconstructed from three-dimensional energy clusters in the calorimeter [62] with the anti-k_t jet clustering algorithm [63] with a radius parameter $R = 0.4$. In the diphoton analysis, only jet candidates with $p_{\mathrm{T}} > 30$ GeV and $|\eta| < 2.8$ are considered. For jets used in the photon+jets analysis, the acceptance is further reduced to $|\eta| < 2.5$. Jets are calibrated as described in Refs. [64, 65], with the expected average energy contribution from pileup clusters subtracted in accordance with the angular area of the jet. Jets resulting from the hadronization of b-quarks are identified using the multivariate MV2c10 b-tagging algorithm, which is based on quantities such as impact parameters of associated tracks, and reconstructed secondary vertices [66, 67]. This algorithm is used at a working point that provides 77% b-tagging efficiency in simulated $t\bar{t}$ events, and a rejection factor of 134 for light-quark and gluon jets and 6 for charm jets.

To avoid ambiguity that arises when an electron or photon is also reconstructed as a jet, the following procedure is used: if a jet and an electron or photon are reconstructed within a phase-space separation of $\Delta R_y = 0.2$ of one another, the electron or photon is retained and the jet is discarded; if $0.2 < \Delta R_y < 0.4$ then the jet is retained and the electron or photon is discarded. Finally, in order to suppress the reconstruction of muons arising from showers induced by jets, if a jet and a muon are found with $\Delta R_y < 0.4$ the jet is retained and the muon is discarded.

The vector momentum imbalance $\vec{E}_{\mathrm{T}}^{\mathrm{miss}}$ in the transverse plane is obtained from the negative vector sum of the reconstructed and calibrated physics objects, and an additional soft term. The soft term is constructed from all tracks that are not associated with any reconstructed electron, muon or jet, but which are associated with the primary vertex.

Several additional observables are defined to help in the discrimination of SM backgrounds from potential GGM signals. The total visible transverse energy H_{T} is defined as the scalar sum of the transverse momenta of the selected photons and any additional leptons and jets in the event. The "effective mass" m_{eff} is defined as the scalar sum of H_{T} and $E_{\mathrm{T}}^{\mathrm{miss}}$. Requiring a minimum value for either of these observables exploits the high energy scale associated with the production of massive SUSY partners. The photon–$E_{\mathrm{T}}^{\mathrm{miss}}$ separation $\Delta\phi(\gamma, E_{\mathrm{T}}^{\mathrm{miss}})$ is defined as the azimuthal angle between the $\vec{E}_{\mathrm{T}}^{\mathrm{miss}}$ vector and the selected photon. In the case of the diphoton analysis, $\Delta\phi_{\mathrm{min}}(\gamma, E_{\mathrm{T}}^{\mathrm{miss}})$ is defined to be the minimum value of $\Delta\phi(\gamma, E_{\mathrm{T}}^{\mathrm{miss}})$ of the two selected photons. The minimum jet–$E_{\mathrm{T}}^{\mathrm{miss}}$ separation $\Delta\phi_{\mathrm{min}}(\mathrm{jet}, E_{\mathrm{T}}^{\mathrm{miss}})$ is defined as the minimum azimuthal angle between the $\vec{E}_{\mathrm{T}}^{\mathrm{miss}}$ vector and the two leading (highest-p_{T}) jets in the event. For the diphoton analysis, leading jets are required to have $p_{\mathrm{T}} > 75$ GeV for the purpose of constructing this observable, and if no such jet is found no requirement is placed on the observable. Small values of these angular-separation observables are often associated with SM backgrounds arising from poorly reconstructed objects. Finally, the quantity R_{T}^4 is defined as the scalar sum of the transverse momenta of the four highest-p_{T} jets in the event divided by the scalar sum of the transverse momenta of all jets in the event; smaller values of R_{T}^4 are typical for the jet-rich events of the higgsino–bino GGM model that is the focus of the photon+jets analysis.

6 Event selection

The data sample is selected by a trigger requiring the presence of one loose photon with $E_{\mathrm{T}} > 140$ GeV for the photon+jets analysis, or two loose photons with $E_{\mathrm{T}} > 35$ GeV and $E_{\mathrm{T}} > 25$ GeV, respectively, for the diphoton analysis. After applying data-quality requirements related to the beam and detector conditions, the total available integrated luminosity is 36.1 fb^{-1}.

For the diphoton analysis, targeting the exploration of the gluino–bino, squark–bino and wino–bino GGM models incorporating a purely bino-like $\tilde{\chi}_1^0$, two separate SR selection strategies are used: a "$\mathrm{SR}_{\mathrm{S}}^{\gamma\gamma}$" selection targeting the production of higher-mass strongly coupled SUSY states (gluinos and squarks) and a "$\mathrm{SR}_{\mathrm{W}}^{\gamma\gamma}$" selection targeting the production of lower-mass weakly coupled SUSY states (winos). For each of these approaches, two SRs are defined: the first ($\mathrm{SR}_{\mathrm{S-L}}^{\gamma\gamma}$, $\mathrm{SR}_{\mathrm{W-L}}^{\gamma\gamma}$) optimized for the case of a lower-mass $\tilde{\chi}_1^0$ and the second ($\mathrm{SR}_{\mathrm{S-H}}^{\gamma\gamma}$, $\mathrm{SR}_{\mathrm{W-H}}^{\gamma\gamma}$) for a higher-mass $\tilde{\chi}_1^0$. For fixed production-scale (gluino, squark, wino) mass, increasing the mass of the bino NLSP increases the energy carried off by the unobserved gravitinos, at the expense of the overall visible energy deposition.

For the photon+jets analysis, targeting the higgsino–bino GGM model, a further two SRs are defined. The first of these ($\mathrm{SR}_{\mathrm{L}}^{\gamma\mathrm{j}}$) is optimized for a high-mass gluino and a low-to-intermediate mass neutralino, for which there is a large mass difference between the gluino and the neutralino. Such events are characterized by large jet multiplicity and exceptional hadronic activity, but moderate missing transverse momentum. The second of these SRs ($\mathrm{SR}_{\mathrm{H}}^{\gamma\mathrm{j}}$) targets the compressed scenario for which the gluino and neutralino masses are close to one another, resulting in lower jet multiplicity and suppressed hadronic activity, while producing harder photons and greater missing transverse momentum.

All four diphoton SRs require two tight, isolated photons with $E_{\mathrm{T}} > 75$ GeV, while $\mathrm{SR}_{\mathrm{L}}^{\gamma\mathrm{j}}$ and $\mathrm{SR}_{\mathrm{H}}^{\gamma\mathrm{j}}$ require a single tight, isolated photon with $E_{\mathrm{T}} > 145$ GeV and $E_{\mathrm{T}} > 400$ GeV, respectively. To exploit the transverse momentum imbalance created by the unobservable gravitinos, an event must exhibit significant $E_{\mathrm{T}}^{\mathrm{miss}}$ to be included in any of the SRs. To ensure that the $E_{\mathrm{T}}^{\mathrm{miss}}$ observable is accurately measured, minimum requirements on $\Delta\phi_{\mathrm{min}}(\gamma, E_{\mathrm{T}}^{\mathrm{miss}})$ and $\Delta\phi_{\mathrm{min}}(\mathrm{jet}, E_{\mathrm{T}}^{\mathrm{miss}})$ are considered for each SR.

Requirements are made on a number of additional observables, defined in Section 5, with values chosen to optimize the sensitivity to the GGM signal of interest in each SR. To exploit the high energy scale associated with SUSY production at masses close to the expected limit of sensitivity of the various SRs, all SRs include minimum requirements on one of the two total-transverse-energy observables H_{T} or m_{eff}. As an illustration, Figure 3 (left) shows the H_{T} distribution of selected diphoton events as well as that expected from SM sources (estimated as described in Section 7) and from four characteristic scenarios of the bino-like NLSP GGM gluino-production model. Due to the large backgrounds arising from SM single-photon production, requirements must be placed on additional observables in order to optimize the signal sensitivity in the photon+jets analysis. A minimum of five (three) jets are required for events in $\mathrm{SR}_{\mathrm{L}}^{\gamma\mathrm{j}}$ ($\mathrm{SR}_{\mathrm{H}}^{\gamma\mathrm{j}}$). For $\mathrm{SR}_{\mathrm{L}}^{\gamma\mathrm{j}}$ of the photon+jets analysis, an additional requirement that events have $R_{\mathrm{T}}^4 < 0.90$ helps reduce the background from SM events, which tend to have fewer and softer jets than do signal events; as an illustration, see Figure 3 (right). Finally, for both $\mathrm{SR}_{\mathrm{L}}^{\gamma\mathrm{j}}$ and $\mathrm{SR}_{\mathrm{H}}^{\gamma\mathrm{j}}$, events with one or more leptons (electron or muon) are rejected in order to suppress the contribution from SM events containing leptonically decaying W or Z bosons produced in association with a hard radiated photon ("$V\gamma$" production). In addition, a predecessor to $\mathrm{SR}_{\mathrm{L}}^{\gamma\mathrm{j}}$, originally designed for a search using a smaller data set (13.2 fb^{-1}), has been retained, as the number of events observed in that search exceeded the background prediction. This third photon+jets SR is referred to as $\mathrm{SR}_{\mathrm{L200}}^{\gamma\mathrm{j}}$, and differs from $\mathrm{SR}_{\mathrm{L}}^{\gamma\mathrm{j}}$ only by the relaxed requirement $E_{\mathrm{T}}^{\mathrm{miss}} > 200$ GeV relative to the $E_{\mathrm{T}}^{\mathrm{miss}} > 300$ GeV requirement of $\mathrm{SR}_{\mathrm{L}}^{\gamma\mathrm{j}}$. A summary of the selection requirements for the various SRs is presented in Table 1.

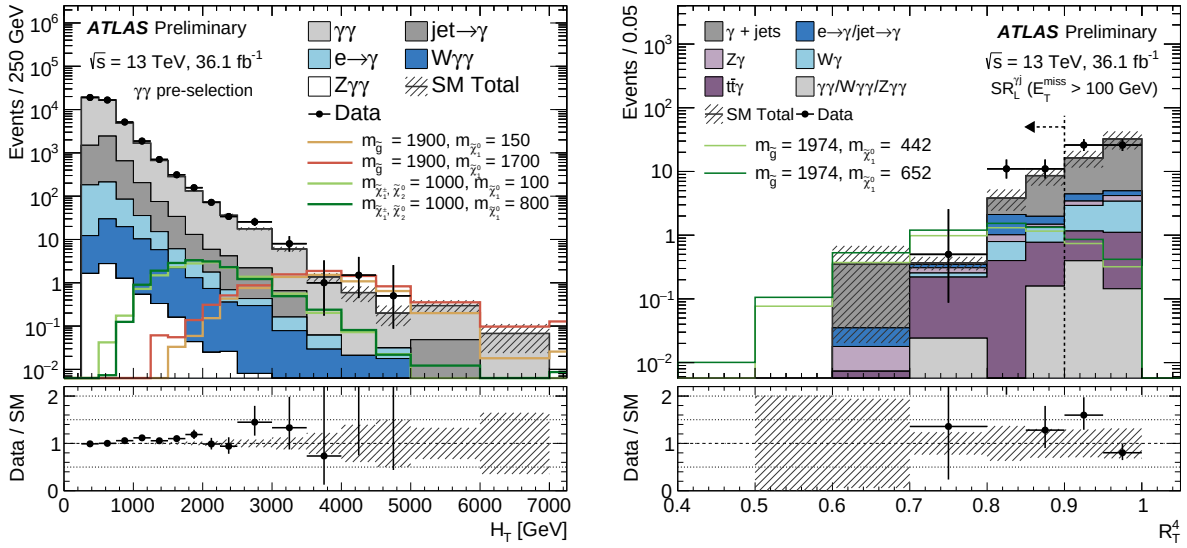

Figure 3: Left: distribution of the total visible transverse energy H_{T} for selected diphoton events, after requiring $\Delta\phi_{\mathrm{min}}(\mathrm{jet}, E_{\mathrm{T}}^{\mathrm{miss}}) > 0.5$ but before application of a requirement on $E_{\mathrm{T}}^{\mathrm{miss}}$ and $\Delta\phi_{\mathrm{min}}(\gamma, E_{\mathrm{T}}^{\mathrm{miss}})$. Also shown are the expected H_{T} distributions of contributing SM processes as well as those for two points each in the parameter spaces of the gluino–bino and wino–bino GGM models. Events outside the range of the displayed region are included in the highest-valued bin. Right: distribution of R_{T}^4 for the sample satisfying all $\mathrm{SR}_{\mathrm{L}}^{\gamma\mathrm{j}}$ selection criteria except the R_{T}^4 requirement itself, but with a relaxed requirement of $E_{\mathrm{T}}^{\mathrm{miss}} > 100$ GeV. Also shown are the expected R_{T}^4 distributions of contributing SM processes as well as those for two points in the $m_{\tilde{g}}$–$m_{\tilde{\chi}_1^0}$ parameter space of the GGM model relevant to the photon+jets analysis. The value of the gluino mass arises from the choice $M_3 = 1900$ GeV, while the values of the $\tilde{\chi}_1^0$ mass arise from the choices $\mu = 400$ and $\mu = 600$ GeV, combined with the constraint that the branching fraction of $\tilde{\chi}_1^0 \to \gamma\tilde{G}$ be 50%. The vertical dashed-and-dotted line and left-pointing arrow shows the region of the R_{T}^4 observable selected for inclusion in $\mathrm{SR}_{\mathrm{L}}^{\gamma\mathrm{j}}$. Uncertainties are shown as hatched bands for the various expected sources of SM background (statistical only) and as error bars for data. The lower panels show the ratio between the data and the SM prediction.

7 Background estimation

Backgrounds to the various SRs arise from a number of sources that generate real photons in combination with energetic neutrinos, as well as events in which one or more energetic jets or electrons are misidentified as photons. In the following, the methodology of the background estimation for the two experimental signatures is discussed, and the resulting background estimates, broken down by source, are tabulated. Backgrounds arising from misidentified jets and electrons are estimated through the use of control samples including jets or electrons, scaled by misidentification rates determined from data. Other backgrounds are estimated via MC simulation, often constrained by observed event counts in dedicated CRs. For the estimation of background contributions that rely upon MC simulation, either directly or through the estimation of "transfer factors" relating the background content of CRs to that of corresponding SRs, the effect of MC modeling uncertainties are considered.

In the case of the photon+jets analysis, expected SM backgrounds constrained by CRs are determined separately for each SR with a maximum likelihood fit, referred to as the "background-only fit". The background-only fit constrains the normalization of the dominant backgrounds to the observed event

Table 1: The requirements defining the seven SRs for the diphoton and photon+jets searches. All symbols are defined in the text. An ellipsis is entered when no such requirement is made in the given signal region.

Signal Region	$SR^{\gamma\gamma}_{S-L}$	$SR^{\gamma\gamma}_{S-H}$	$SR^{\gamma\gamma}_{W-L}$	$SR^{\gamma\gamma}_{W-H}$	$SR^{\gamma j}_{L}$	$SR^{\gamma j}_{L200}$	$SR^{\gamma j}_{H}$
Number of photons	≥ 2	≥ 2	≥ 2	≥ 2	≥ 1	≥ 1	≥ 1
E_T^γ [GeV]	> 75	> 75	> 75	> 75	> 145	> 145	> 400
Number of jets	...	...	...	...	≥ 5	≥ 5	≥ 3
Number of leptons	...	...	...	...	0	0	0
E_T^{miss} [GeV]	> 150	> 250	> 150	> 250	> 300	> 200	> 400
H_T [GeV]	> 2750	> 2000	> 1500	> 1000	...	...	...
m_{eff} [GeV]	...	...	...	...	> 2000	> 2000	> 2400
R_T^4	...	...	...	...	< 0.90	< 0.90	...
$\Delta\phi_{min}$(jet, E_T^{miss})	> 0.5	> 0.5	> 0.5	> 0.5	> 0.4	> 0.4	> 0.4
$\Delta\phi_{min}(\gamma, E_T^{miss})$ ($\Delta\phi(\gamma, E_T^{miss})$)	...	> 0.5	...	> 0.5	(> 0.4)	(> 0.4)	(> 0.4)

yields in the associated CRs, assuming that no signal is present in the CRs. The inputs to the fit for each SR include the numbers of events observed in its associated CRs and the number of events predicted by simulation in each region for all background processes. The latter are described by Poisson statistics. The systematic uncertainties in the expected values are included in the fit as nuisance parameters, modeled by Gaussian distributions with widths corresponding to the sizes of the associated uncertainties. Correlations between the various CRs are taken into account. The product of the various probability density functions forms the likelihood, which the fit maximizes by adjusting the background normalization and the nuisance parameters. Background models are confirmed in validation regions (VRs) with selection criteria closely related to those of the corresponding SR, but with one or more selection criteria modified to suppress the potential contribution of a GGM signal to the VR.

7.1 Backgrounds to the diphoton analysis

Backgrounds from SM contributions to the four diphoton SRs are grouped into three primary components. The first of these, referred to as "QCD background," arises from a mixture of processes that include $\gamma\gamma$ production as well as γ + jet and multijet events with at least one jet mis-reconstructed as a photon. The second background component, referred to as "EW background," is due primarily to $W + X$ (here "X" can be any number of jets, accompanied by no more than one photon; the two-photon case is treated separately) and $t\bar{t}$ events. These events tend to include final-state neutrinos that produce significant E_T^{miss}. In both cases, EW background events entering the signal regions generally have at least one electron mis-reconstructed as a photon. The QCD and EW backgrounds are estimated through the use of dedicated control samples of data events.

The third background component, referred to as "irreducible," consists of W and Z bosons produced in association with two real photons, with a subsequent decay into one or more neutrinos. For this background, the $W(\rightarrow \ell\nu) + \gamma\gamma$ component dominates, and requires corrections to its LO contribution that are both large and rapidly varying across the phase space of the $W(\rightarrow \ell\nu)+\gamma\gamma$ (plus possible additional

jets) process [68]. Thus a data-driven approach is developed to constrain the $W(\to \ell\nu) + \gamma\gamma$ contribution to the four SRs. The $Z(\to \nu\bar{\nu}) + \gamma\gamma$ contribution is estimated directly from the MC simulation.

The QCD background to $\mathrm{SR}^{\gamma\gamma}_{\mathrm{S-L}}$, $\mathrm{SR}^{\gamma\gamma}_{\mathrm{S-H}}$, $\mathrm{SR}^{\gamma\gamma}_{\mathrm{W-L}}$ and $\mathrm{SR}^{\gamma\gamma}_{\mathrm{W-H}}$ is expected to arise from events with a single real, isolated photon and a jet whose fragmentation fluctuates in such a manner as to cause it to be misidentified as a second isolated photon ("jet $\to \gamma$" events), and, to a lesser extent, from events with two real, isolated photons unaccompanied by any additional electroweak bosons ("QCD diphoton" events). The contribution from dijet events is found to be small and largely incorporated into the jet $\to \gamma$ background estimate.

To estimate the jet $\to \gamma$ contribution, a "QCD control sample" is identified within the diphoton-trigger data sample by selecting events for which one photon candidate satisfies the tight selection criterion, while the other satisfies the loose but not the tight photon criterion. Both photons are required to have $E_{\mathrm{T}}^{\gamma} > 75$ GeV, and events containing electrons are vetoed to reduce contamination from $W \to e\nu$ decays. A model of the jet $\to \gamma$ background is then obtained by multiplying the number of control-sample events by a loose-to-tight scale factor of between 0.1 and 0.5, depending upon the values of p_{T} and η of the loose photon, determined from events with poorly isolated photons ($10 < E_{\mathrm{T}}^{0.4} - 0.22 \times E_{\mathrm{T}}^{\gamma} < 30$ GeV). Studies with MC simulated samples as well as $E_{\mathrm{T}}^{\mathrm{miss}}$ and H_{T} sideband data show this sample to be dominated by mis-reconstructed particles in hadronic jets, and also suggest that the $E_{\mathrm{T}}^{\mathrm{miss}}$ distribution of this control sample adequately reproduces the $E_{\mathrm{T}}^{\mathrm{miss}}$ distribution of the QCD background in the high-$E_{\mathrm{T}}^{\mathrm{miss}}$ region used for the signal selection.

A diphoton MC sample, scaled as a function of $E_{\mathrm{T}}^{\mathrm{miss}}$ and the number of jets to reproduce the observed numbers of data events in the region $0 < E_{\mathrm{T}}^{\mathrm{miss}} < 150$ GeV, is used for the estimation of the small diphoton contribution to the QCD background. Before the application of a requirement on H_{T}, and for each bin in the number of observed jets, an $E_{\mathrm{T}}^{\mathrm{miss}}$-dependent scale factor is applied to the MC simulation to establish agreement between data and simulation. The scaling behavior for values of $E_{\mathrm{T}}^{\mathrm{miss}}$ in the diphoton SRs is estimated by extrapolating the $E_{\mathrm{T}}^{\mathrm{miss}}$ dependences of the scale factors observed for $E_{\mathrm{T}}^{\mathrm{miss}} < 150$ GeV into the region $E_{\mathrm{T}}^{\mathrm{miss}} > 150$ GeV. This procedure yields the agreement between the data and MC distributions of H_{T} illustrated in Figure 3.

For each SR, the jet $\to \gamma$ (QCD diphoton) background estimate is obtained by counting the number of scaled QCD control (diphoton MC) events satisfying the combined $E_{\mathrm{T}}^{\mathrm{miss}}$, H_{T} and $\Delta\phi$ requirements for the given SR. The statistical uncertainty in each estimate is determined according to the unscaled number of events in the QCD control and diphoton MC samples that satisfy these requirements. For the case that no events remain in the given sample, a one-sided statistical uncertainty is adopted, corresponding to the 68% confidence level (CL) Poisson upper limit on the possible background contribution. An additional uncertainty of ±50% is included to account for possible modeling uncertainties. The resulting QCD background estimates and their overall uncertainties are shown in Table 2, separately for the jet $\to \gamma$ and QCD diphoton contributions.

The EW background is estimated via an "electron–photon control sample" composed of events with at least one isolated tight photon and one isolated electron, each with $E_{\mathrm{T}} > 75$ GeV; when there is more than one identified electron, the one with the highest p_{T} is used. The electron–photon control sample is scaled by the probability for such an electron to be mis-reconstructed as a tight photon, as estimated from a comparison of the rate of Z boson reconstruction in the $e\gamma$ and ee final states. The electron-to-photon scale factor varies between 1% and 5%, with larger factors associated with larger values of $|\eta|$, since the misidentification rate depends on the amount of material in front of the calorimeter. Events with additional photons or leptons are vetoed from the control sample to preserve its orthogonality to the various diphoton

Table 2: The expected and observed numbers of events for the four diphoton signal regions. The quoted errors are the combined statistical and systematic uncertainties.

Signal Region	$SR^{\gamma\gamma}_{S-L}$	$SR^{\gamma\gamma}_{S-H}$	$SR^{\gamma\gamma}_{W-L}$	$SR^{\gamma\gamma}_{W-H}$
jet $\to \gamma$	$0.19^{+0.21}_{-0.19}$	$0.19^{+0.21}_{-0.19}$	0.93 ± 0.67	$0.19^{+0.21}_{-0.19}$
QCD diphoton	$0.00^{+0.17}_{-0.00}$	$0.00^{+0.17}_{-0.00}$	$0.15^{+0.17}_{-0.15}$	$0.00^{+0.17}_{-0.00}$
EW background	0.08 ± 0.04	0.06 ± 0.04	0.88 ± 0.23	0.51 ± 0.15
$(W \to \ell\nu)\gamma\gamma$	0.22 ± 0.14	0.21 ± 0.13	1.55 ± 0.78	1.08 ± 0.56
$(Z \to \nu\nu)\gamma\gamma$	0.01 ± 0.01	0.03 ± 0.02	0.15 ± 0.08	0.27 ± 0.13
Expected background events	$0.50^{+0.30}_{-0.26}$	$0.48^{+0.30}_{-0.25}$	3.67 ± 1.07	$2.05^{+0.65}_{-0.63}$
Observed events	0	0	6	1

and photon+jets SRs. After applying all additional selection requirements to the scaled electron–photon control sample, and including a systematic uncertainty of ±20% associated with the determination of the scale factor, the resulting estimates of the EW background to the four diphoton SRs are shown in Table 2.

The $W(\to \ell\nu) + \gamma\gamma$ background to the four diphoton SRs is estimated using a lepton–diphoton ($\ell\gamma\gamma$) CR. To enhance the contribution of $W(\to \ell\nu) + \gamma\gamma$ and to ensure that the $\ell\gamma\gamma$ CR is exclusive of the four SRs, the photon E_{T} requirement is lowered to 50 GeV and a requirement of $50 < E_{\mathrm{T}}^{\mathrm{miss}} < 150$ GeV is imposed. To ensure that the CR sample arises from the same region of the $W(\to \ell\nu) + \gamma\gamma$ process phase space as the expected background, a further requirement that the transverse momentum of the $\ell\gamma\gamma$ system be greater than 100 GeV is imposed. A total of 13 events is observed in the CR, for which MC simulation suggests that 3.9 events are expected to arise from SM sources other than $W(\to \ell\nu) + \gamma\gamma$. In the limit that no GGM signal contributes to the $\ell\gamma\gamma$ control region, an enhancement factor of $1.6 \pm 0.6 \pm 0.4$ must be applied to the $W(\to \ell\nu) + \gamma\gamma$ MC sample to achieve agreement between the MC simulation and data in the $\ell\gamma\gamma$ control region. The statistical uncertainty of ±0.6 arises from the Poisson error on the difference between the observed number of events in the $\ell\gamma\gamma$ control region and the number of events expected from SM processes other than $W(\to \ell\nu) + \gamma\gamma$ production. The systematic uncertainty of ±0.4 arises from assuming that the non-$W(\to \ell\nu) + \gamma\gamma$ contributions to the $\ell\gamma\gamma$ CR are 100% uncertain; this uncertainty dominates smaller contributions arising from potential mis-modeling of the ATLAS detector response. For each diphoton SR, the $W(\to \ell\nu) + \gamma\gamma$-background estimate is then provided by applying all associated SR requirements to the scaled $W(\to \ell\nu) + \gamma\gamma$ MC sample. The resulting $W(\to \ell\nu) + \gamma\gamma$-background estimate in each of the four SRs, under the assumption that there is no signal contribution to the $\ell\gamma\gamma$ CR, is shown in Table 2. Also shown is the combined background estimate, including uncertainty, from all SM sources; for the case of the $Z(\to \nu\bar{\nu}) + \gamma\gamma$ background, an uncertainty of ±45% is assigned to account for the effect of QCD scale dependence associated with the limited-order simulation of the $Z(\to \nu\bar{\nu}) + \gamma\gamma$ process discussed in Section 4.

The accuracy of the resulting overall background model is confirmed by the use of seven VRs that, while excluding events in the four diphoton SRs, have similar kinematic properties to those of the signal region. The definitions of these VRs are shown in Table 3, together with the expected and observed numbers of events in each region. Figure 4 also shows this comparison, with the expected number of events broken

down into its contributing SM sources.

Figure 5 shows the distribution of the missing transverse momentum $E_{\mathrm{T}}^{\mathrm{miss}}$ for the sample satisfying all requirements of the $\mathrm{SR}^{\gamma\gamma}_{\mathrm{W-H}}$ (left) and $\mathrm{SR}^{\gamma\gamma}_{\mathrm{W-L}}$ (right) selection except the $E_{\mathrm{T}}^{\mathrm{miss}}$ requirement itself. Overlaid are the expected SM backgrounds, separated into the various contributing sources.

Table 3: Definition, expected content and observed content of the seven validation regions used to confirm the diphoton analysis background model. Here, N_{lep} is the number of required leptons of the stated type, and N_{exp} and N_{obs} are the expected and observed numbers of events, respectively. The remainder of the quantities are defined the the text. The uncertainties on the numbers of expected events are the combined statistical and systematic uncertainties. An ellipsis is entered when no such requirement is made of the given validation region.

	E_{T}^{γ} [GeV]	$\Delta\phi_{\mathrm{min}}(\mathrm{jet}, E_{\mathrm{T}}^{\mathrm{miss}})$	N_{lep}	H_{T} [GeV]	$E_{\mathrm{T}}^{\mathrm{miss}}$ [GeV]	N_{exp}	N_{obs}
$\mathrm{VR1}^{\gamma\gamma}$	> 75	> 0.5	...	...	< 150	43524 ± 4388	43918
$\mathrm{VR2}^{\gamma\gamma}$	> 75	> 0.5	...	$(1000, 2500)$	< 150	2845 ± 522	3139
$\mathrm{VR3}^{\gamma\gamma}$	> 75	> 0.5	...	...	$(100, 150)$	112 ± 36	109
$\mathrm{VR4}^{\gamma\gamma}$	> 50	...	$1e$	< 2000	...	34.5 ± 7.2	38
$\mathrm{VR5}^{\gamma\gamma}$	> 50	...	1μ	< 2000	...	19.8 ± 7.1	25
$\mathrm{VR6}^{\gamma\gamma}$	> 75	> 0.5	...	> 1750	...	287 ± 129	336
$\mathrm{VR7}^{\gamma\gamma}$	> 75	> 0.5	...	...	> 100	139 ± 40	146

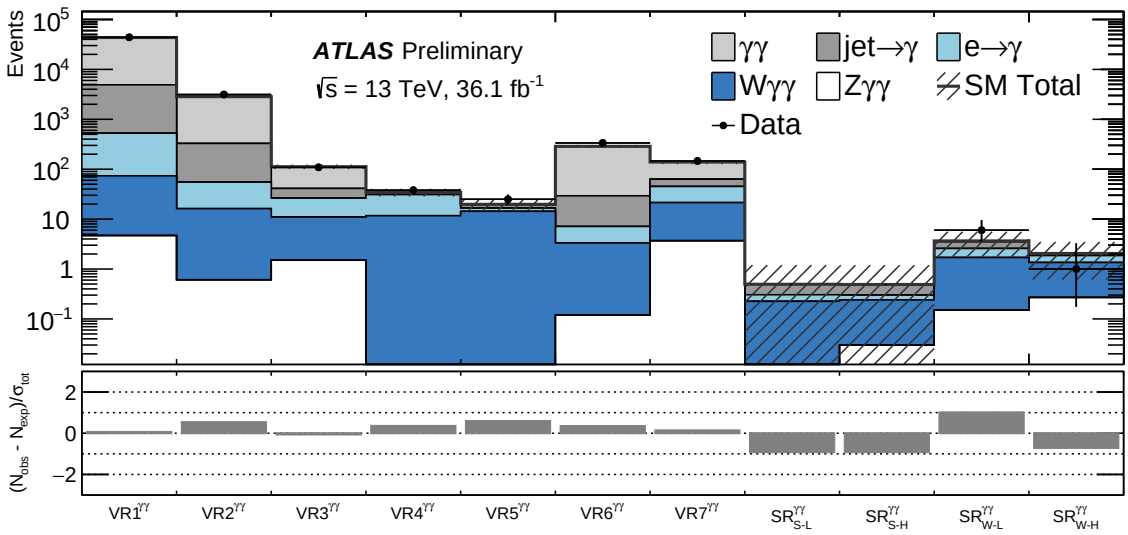

Figure 4: Comparisons between expected and observed content of the validation and signal regions for the diphoton analysis. The uncertainties on the numbers of expected events are the combined statistical and systematic uncertainties. The lower panel shows the pull (difference between observed and expected event counts normalized by the uncertainty) for each region.

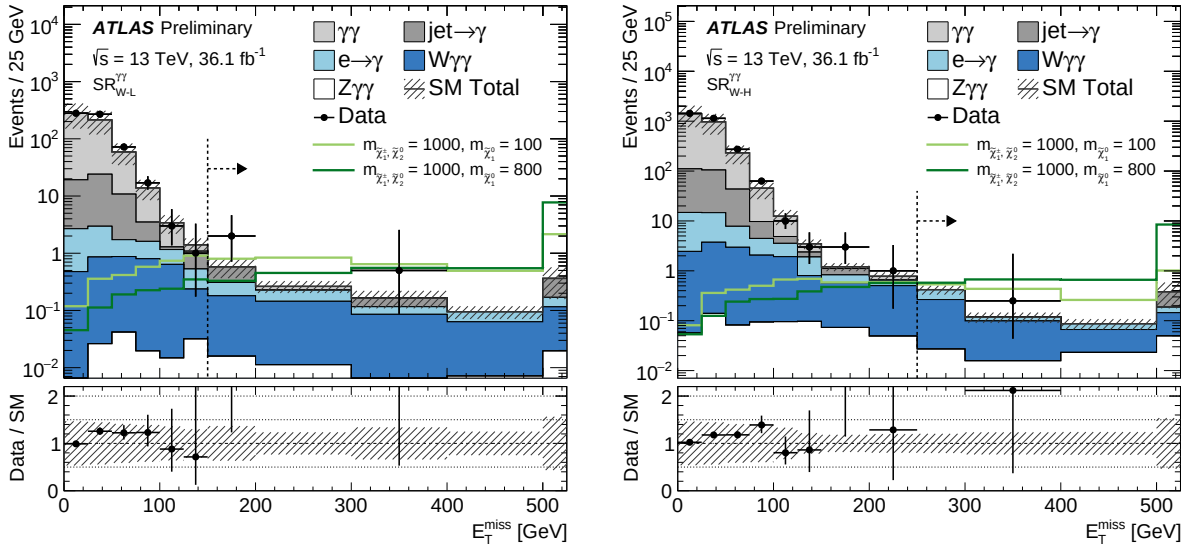

Figure 5: Distribution of the missing transverse momentum $E_{\mathrm{T}}^{\mathrm{miss}}$ for the sample satisfying all requirements of the (left) $\mathrm{SR}^{\gamma\gamma}_{\mathrm{W-L}}$ and (right) $\mathrm{SR}^{\gamma\gamma}_{\mathrm{W-H}}$ selection except the $E_{\mathrm{T}}^{\mathrm{miss}}$ requirement itself. Overlaid are the expected SM backgrounds, separated into the various contributing sources. Also shown are the signal expectations for the $(m_{\tilde{W}}, m_{\tilde{\chi}_1^0}) = (1000, 100)$ GeV and $(m_{\tilde{W}}, m_{\tilde{\chi}_1^0}) = (1000, 800)$ GeV models. The vertical dashed-and-dotted lines and right-pointing arrows show the region of the $E_{\mathrm{T}}^{\mathrm{miss}}$ observable selected for inclusion in $\mathrm{SR}^{\gamma\gamma}_{\mathrm{W-L}}$ and $\mathrm{SR}^{\gamma\gamma}_{\mathrm{W-H}}$. The lower panels show the ratio of observed data to the combined SM expectation. For these plots, the band represents the range of combined statistical and systematic uncertainty on the SM expectation. Events outside the range of the displayed region are included in the highest-valued bin.

7.2 Backgrounds to the photon+jets analysis

Backgrounds from SM contributions to the three photon+jets SRs are expected to arise both from events with real photons as well as events for which an electron or a jet is misidentified as a photon. The former source is expected to receive contributions from events for which a W/Z boson, a single top quark, or a $t\bar{t}$ pair is produced in association with a real photon ($W\gamma$, $Z\gamma$ and $t\bar{t}\gamma$ background), with neutrinos in the subsequent weak decays of these produced states providing significant $E_{\mathrm{T}}^{\mathrm{miss}}$. Events with real photons can also contribute to the background in the photon+jets analysis when significant $E_{\mathrm{T}}^{\mathrm{miss}}$ arises from instrumental sources (QCD background). The $W\gamma$, $t\bar{t}\gamma$ and QCD backgrounds are estimated by constraining a corresponding MC sample to match the observed event count in a dedicated CR enriched in the given background process but otherwise kinematically similar to the given SR, making use of the maximum likelihood approach described at the beginning of this section. The MC simulation is then used to provide an estimate of the expected background in the photon+jets SRs. Smaller contributions from $Z\gamma$ and $\gamma\gamma$ (with or without an accompanying W or Z boson) production are estimated directly from the MC simulation. The methods used to estimate contributions from events for which electrons ("$e \to \gamma$" backgrounds) or jets ("jet $\to \gamma$" backgrounds) are misidentified as photons are identical to those used in the diphoton analysis, with the exception that the single-photon trigger sample is used instead of the diphoton trigger sample, the requirement that the electron or loose photon be accompanied by a tight isolated photon is removed, and the requirement for photons to be considered poorly isolated is changed to $8 < E_{\mathrm{T}}^{0.4} - 0.22 \times E_{\mathrm{T}}^{\gamma} - 2.45 < 27$ GeV.

All CRs require at least one isolated photon with $E_{\mathrm{T}} > 145$ GeV. The QCD-background control region $\mathrm{CR}_{\gamma+\mathrm{jets}}$ is similar to $\mathrm{SR}_{\mathrm{L}}^{\gamma\mathrm{j}}$, but with the $E_{\mathrm{T}}^{\mathrm{miss}}$ requirement lowered to $E_{\mathrm{T}}^{\mathrm{miss}} > 100$ GeV, the R_{T}^{4} requirement removed, the number of required jets lowered to three, and the $\Delta\phi_{\mathrm{min}}(\mathrm{jet}, E_{\mathrm{T}}^{\mathrm{miss}})$ requirement inverted. This provides a region dominated by real photons arising from radiative QCD processes that is otherwise fairly similar to the photon+jets SRs. The $W\gamma$-background control region $\mathrm{CR}_{W\gamma}$ is defined by requiring that there be one or more isolated leptons (electron or muon), at least one jet, and no b-tagged jet in the event. In addition, the $E_{\mathrm{T}}^{\mathrm{miss}}$ requirement is changed to $100 < E_{\mathrm{T}}^{\mathrm{miss}} < 200$ GeV and the m_{eff} requirement reduced to $m_{\mathrm{eff}} > 500$ GeV in order to enhance and isolate the $W\gamma$ contribution. The $t\bar{t}\gamma$-background control region $\mathrm{CR}_{t\bar{t}\gamma}$ is defined similarly, but requires at least two jets, and that two of the jets are b-tagged jets. In order to increase the number of events in the CR the $E_{\mathrm{T}}^{\mathrm{miss}}$ requirement is lowered to $50 < E_{\mathrm{T}}^{\mathrm{miss}} < 200$ GeV. Both the $W\gamma$-background and $t\bar{t}\gamma$-background CRs maintain the requirement $\Delta\phi_{\mathrm{min}}(\mathrm{jet}, E_{\mathrm{T}}^{\mathrm{miss}}) > 0.4$. Table 4 summarizes the selection criteria for the three photon+jets analysis CRs.

Table 4: Selection criteria for the three photon+jets analysis control regions. Here, N_γ is the number of required photons, E_{T}^{γ} the transverse energy of the leading photon, N_{lep} the number of required leptons, N_{jets} the number of required jets, and $N_{b-\mathrm{jets}}$ the number of require b-quark jets. The remainder of the quantities are defined the the text. An ellipsis is entered when no such requirement is made in the given control region.

	$\mathrm{CR}_{\gamma+\mathrm{jets}}$	$\mathrm{CR}_{W\gamma}$	$\mathrm{CR}_{t\bar{t}\gamma}$
N_γ	≥ 1	≥ 1	≥ 1
E_{T}^{γ}	> 145 GeV	> 145 GeV	> 145 GeV
N_{lep}	0	≥ 1	≥ 1
$E_{\mathrm{T}}^{\mathrm{miss}}$	> 100 GeV	$[100 - 200]$ GeV	$[50 - 200]$ GeV
N_{jets}	≥ 3	≥ 1	≥ 2
$N_{b-\mathrm{jets}}$	...	0	≥ 2
$\Delta\phi(\mathrm{jet}, E_{\mathrm{T}}^{\mathrm{miss}})$	< 0.4	> 0.4	> 0.4
$\Delta\phi(\gamma, E_{\mathrm{T}}^{\mathrm{miss}})$	> 0.4	...	...
m_{eff}	> 2000 GeV	> 500 GeV	> 500 GeV

The event counts in the resulting QCD, $W\gamma$ and $t\bar{t}\gamma$ CRs are used to scale the γ+jet, $W\gamma$ and $t\bar{t}\gamma$ MC samples, respectively, after applying a selection identical to that of the corresponding CR. The scale factors are determined in a simultaneous fit to all CRs, taking into account mutual cross contamination between the different backgrounds. The scale factors (ratio of the derived background contribution in the corresponding control region to the MC expectation) are found to be 1.67 ± 0.49, 1.24 ± 0.11 and 1.20 ± 0.17 for the QCD, $W\gamma$ and $t\bar{t}\gamma$ backgrounds, respectively. The resulting SR contributions from the QCD, $W\gamma$ and $t\bar{t}\gamma$ processes depend upon transfer factors, given by MC simulation, that relate the contribution of a given background process in the CR to that in the SR. Uncertainties in the transfer factors include those arising from experimental uncertainties in object identification and energy measurement, as well as theoretical uncertainties that are estimated by varying the underlying PDF set and renormalization and factorization scales used in the generation of the MC background samples. These uncertainties are incorporated in the overall background estimate uncertainties that arise from the simultaneous fit. Estimates for the contributions of the three real-photon backgrounds are shown in Table 5, with the overall uncertainty taking into account correlations between the various background sources. For the three photon+jets SRs, the systematic uncertainty in each background estimate is dominated by the theoretical uncertainties in the relevant MC samples and the experimental uncertainties in the jet energy scale and resolution.

The accuracy of the resulting photon+jets analysis background model is confirmed by the use of eleven

Table 5: The expected and observed numbers of events in the photon+jets signal regions. The quoted errors are the combined statistical and systematic uncertainties.

Signal Region	$SR_L^{\gamma j}$	$SR_{L200}^{\gamma j}$	$SR_H^{\gamma j}$
γ + jets (QCD)	$0.00^{+0.21}_{-0.00}$	$0.42^{+0.43}_{-0.42}$	0.14 ± 0.14
$W\gamma$	0.54 ± 0.24	0.81 ± 0.22	0.40 ± 0.26
$Z\gamma$	0.31 ± 0.16	0.36 ± 0.13	0.42 ± 0.19
$t\bar{t}\gamma$	0.30 ± 0.11	0.54 ± 0.17	0.07 ± 0.03
$e \to \gamma$	0.07 ± 0.03	0.16 ± 0.06	0.04 ± 0.04
jet $\to \gamma$	$0.07^{+0.44}_{-0.07}$	$0.35^{+0.36}_{-0.35}$	$0.01^{+0.50}_{-0.01}$
$\gamma\gamma/W\gamma\gamma/Z\gamma\gamma$	0.03 ± 0.01	0.03 ± 0.01	0.06 ± 0.02
Expected background events	$1.33^{+0.58}_{-0.32}$	$2.68^{+0.64}_{-0.63}$	$1.14^{+0.61}_{-0.36}$
Observed events	4	8	3

VRs. Similar to the diphoton analysis VRs, these VRs exclude events in the various photon+jets SRs while having similar kinematic properties to those of the signal region. Validation regions $VR1^{\gamma j}$ through $VR6^{\gamma j}$, defined in Table 6, target the confirmation of the modeling of backgrounds arising from γ+jets production. Validation regions $VR7^{\gamma j}$ through $VR11^{\gamma j}$, defined in Table 7, target the confirmation of the modeling of backgrounds arising from $W\gamma$ and $t\bar{t}\gamma$ production and from the misidentification of electrons as photons. Figure 6 shows the comparison between the expected and observed content in the VRs, with the expected content broken down into its contributing SM sources.

Table 6: Definition, expected content and observed content of the six validation regions used to confirm the accuracy of the modeling of the γ + jets background to the photon+jets analysis. Here, E_T^{γ} is the transverse energy of the leading photon, N_{lep} the number of required leptons, N_{jets} the number of required jets, and N_{exp} and N_{obs} are the expected and observed numbers of events, respectively. The remainder of the quantities are defined the the text. The uncertainties in the numbers of expected events are the combined statistical and systematic uncertainties. An ellipsis is entered when no such requirement is made in the given validation region.

	$VR1^{\gamma j}$	$VR2^{\gamma j}$	$VR3^{\gamma j}$	$VR4^{\gamma j}$	$VR5^{\gamma j}$	$VR6^{\gamma j}$
E_T^{γ} (GeV)	> 145	> 145	> 145	> 400	> 400	> 400
N_{lep}	0	0	0	0	0	0
N_{jets}	≥ 5	≥ 5	≥ 5	≥ 3	≥ 3	≥ 3
$\Delta\phi(\text{jet}, E_T^{miss})$	> 0.4	> 0.4	> 0.4	> 0.4	> 0.4	> 0.4
$\Delta\phi(\gamma, E_T^{miss})$	> 0.4	> 0.4	> 0.4	> 0.4	> 0.4	> 0.4
E_T^{miss} (GeV)	[50, 175]	[75, 175]	[100, 175]	[100, 175]	[125, 175]	[150, 175]
m_{eff} (GeV)	> 2000	> 2000	> 2000	> 2000	> 2000	> 2000
R_T^4	< 0.90	< 0.90	< 0.90	...	...	...
N_{exp}	112 ± 20	42 ± 11	10.9 ± 4.1	120 ± 36	36.6 ± 9.9	13.4 ± 5.5
N_{obs}	108	41	15	126	40	10

Figure 7 shows the distribution of the missing transverse momentum E_T^{miss} for the sample satisfying all requirements of the $SR_H^{\gamma j}$ (left) and $SR_L^{\gamma j}$ or $SR_{L200}^{\gamma j}$ (right) selection except the E_T^{miss} requirement itself.

Table 7: Definition, expected content and observed content of the five validation regions used to confirm the accuracy of the modeling of the $W\gamma$, $t\bar{t}\gamma$ and electron-to-photon misidentification backgrounds to the photon+jets analysis. Here, E_{T}^{γ} is the transverse energy of the leading photon, N_{lep} the number of required leptons, N_{jets} the number of required jets, $N_{b-\mathrm{jets}}$ the number of required b-quark jets, and N_{exp} and N_{obs} are the expected and observed numbers of events, respectively. The remainder of the quantities are defined the the text. The uncertainties in the numbers of expected events are the combined statistical and systematic uncertainties. An ellipsis is entered when no such requirement is made in the given validation region.

	VR7$^{\gamma\mathrm{j}}$	VR8$^{\gamma\mathrm{j}}$	VR9$^{\gamma\mathrm{j}}$	VR10$^{\gamma\mathrm{j}}$	VR11$^{\gamma\mathrm{j}}$
E_{T}^{γ} (GeV)	> 145	> 145	> 145	> 145	> 145
N_{lep}	≥ 1	≥ 1	≥ 1	≥ 1	...
N_{jets}	≥ 2	≥ 2	≥ 2	≥ 2	≥ 1
$N_{b-\mathrm{jets}}$	...	...	...	...	≥ 1
$\Delta\phi(\mathrm{jet}, E_{\mathrm{T}}^{\mathrm{miss}})$	> 0.4	> 0.4	> 0.4	< 0.4	> 0.4
$\Delta\phi(\gamma, E_{\mathrm{T}}^{\mathrm{miss}})$	...	...	...	...	< 0.4
$E_{\mathrm{T}}^{\mathrm{miss}}$ (GeV)	< 200	< 200	> 200	> 200	> 200
m_{eff} (GeV)	> 1000	> 1500	[1000, 2000]	> 1500	[500, 2000]
N_{exp}	408 ± 79	66 ± 12	127 ± 23	12.1 ± 2.1	87 ± 12
N_{obs}	410	59	129	11	94

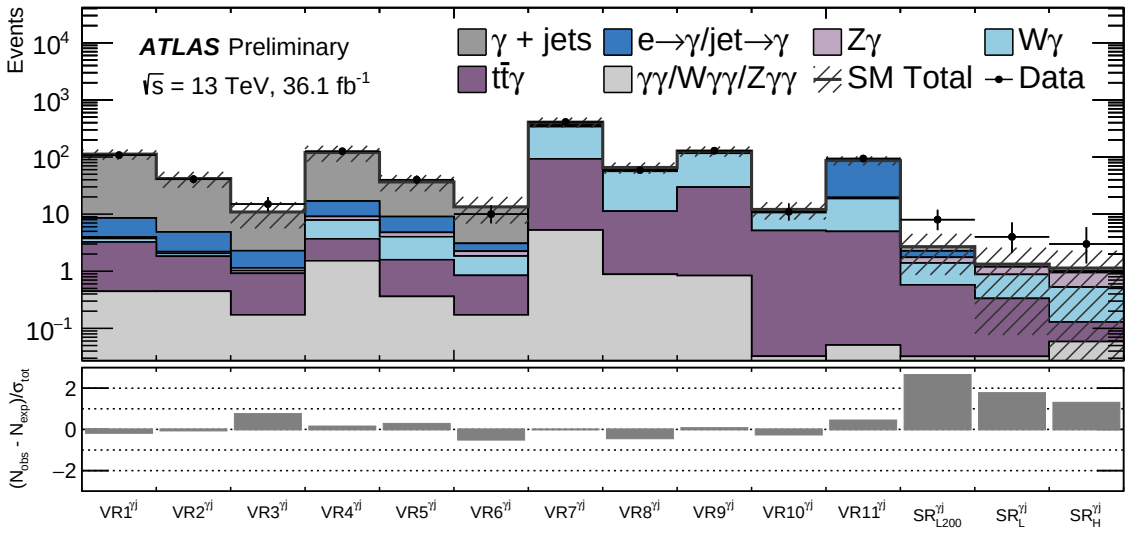

Figure 6: Comparisons between expected and observed content of the validation and signal regions for the photon+jets analysis. The uncertainties in the numbers of expected events are the combined statistical and systematic uncertainties. The lower panel shows the pull (difference between observed and expected event counts normalized by the uncertainty) for each region.

Overlaid are the expected SM backgrounds, separated into the various contributing sources.

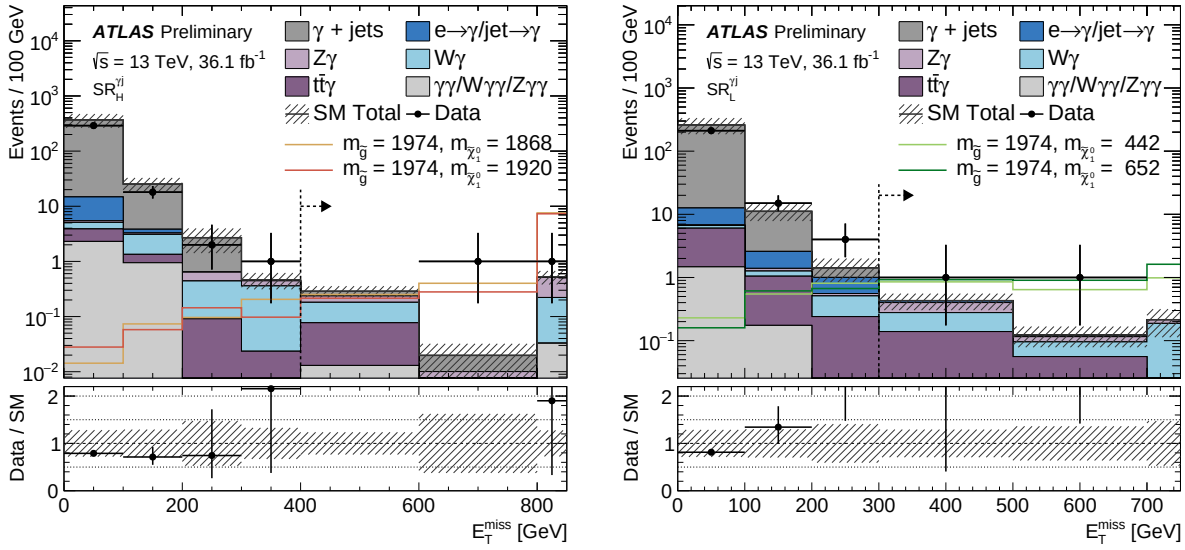

Figure 7: Distribution of the missing transverse momentum $E_{\mathrm{T}}^{\mathrm{miss}}$ for the sample satisfying all requirements of the (left) $\mathrm{SR}_{\mathrm{H}}^{\gamma\mathrm{j}}$ and (right) $\mathrm{SR}_{\mathrm{L}}^{\gamma\mathrm{j}}$ or $\mathrm{SR}_{\mathrm{L200}}^{\gamma\mathrm{j}}$ selection except the $E_{\mathrm{T}}^{\mathrm{miss}}$ requirement itself. Overlaid are the expected SM backgrounds, separated into the various contributing sources. Also shown are the signal expectations for points in the $m_{\tilde{g}}$–$m_{\tilde{\chi}_1^0}$ parameter space of the GGM model relevant to the photon+jets analysis. The value of the gluino mass arises from the choice $M_3 = 1900$ GeV. The $\tilde{\chi}_1^0$ mass values of 1868, 1920, 442 and 652 GeV arise from the choices $\mu = 1810$, 1868, 400 and 600 GeV, respectively, combined with the constraint that the branching fraction of $\tilde{\chi}_1^0 \to \gamma\tilde{G}$ be 50%. The vertical dashed-and-dotted lines and right-pointing arrows show the region of the $E_{\mathrm{T}}^{\mathrm{miss}}$ observable selected for inclusion in $\mathrm{SR}_{\mathrm{H}}^{\gamma\mathrm{j}}$ and $\mathrm{SR}_{\mathrm{L}}^{\gamma\mathrm{j}}$; for $\mathrm{SR}_{\mathrm{L200}}^{\gamma\mathrm{j}}$, the $E_{\mathrm{T}}^{\mathrm{miss}}$ requirement is 200 GeV rather then 300 GeV. The lower panels show the ratio of observed data to the combined SM expectation. For these plots, the band represents the range of statistical uncertainty on the SM expectation. Events outside the range of the displayed region are included in the highest-valued bin.

8 Signal yield and associated uncertainties

GGM signal acceptances and efficiencies are estimated using MC simulation for each simulated point in the gluino–bino, wino–bino, squark–bino and higgsino–bino parameter spaces, and vary widely across the regions of these spaces relevant to establishing the model constraints presented below. The product of acceptance times efficiency tends to be greatest (30–35%) when the masses of both the produced and the NLSP states are largest, leading to large amounts of both visible energy and missing transverse momentum that would clearly distinguish signal from background events. However, for the more restrictive selection of the photon+jets analysis, particularly for the case of a low-mass NLSP, the product of acceptance times efficiency can be significantly smaller. For example, for the region relevant to establishing limits at low values of $m_{\tilde{\chi}_1^0}$, the acceptance-times-efficiency of the $\mathrm{SR}_{\mathrm{L}}^{\gamma\mathrm{j}}$ selection is of the order of 0.1%, leading to a relatively modest constraint on the mass of produced SUSY states.

The MC-based estimate of the signal yield is affected by various experimental systematic uncertainties, described below. The resulting experimental systematic uncertainty in the signal yield is incorporated in the determination of limits on the mass parameters of the various GGM signal models considered in this search.

The uncertainty in the integrated luminosity is 2.1%. It is derived, following a methodology similar to that detailed in Ref. [69], from a calibration of the luminosity scale using x–y beam-separation scans performed in August 2015 and May 2016. Making use of a bootstrap method, the efficiency of the single-photon trigger is determined to be greater than 99%, with an uncertainty of less than ±1%, for photons satisfying the photon+jets selection criteria [29]. The diphoton trigger efficiency is found to be close to 100% for events satisfying the diphoton analysis selection criteria, with an uncertainty of less than 0.4%.

The η-dependent uncertainty in the efficiency of photon identification, determined as described in Ref. [59], is between ±0.2% and ±0.4% for $E_{\mathrm{T}}^{\gamma} < 200$ GeV, and between ±1% and ±4% for larger values of E_{T}^{γ}. The uncertainty in the energy scale for electromagnetic objects with high E_{T}, determined as described in Ref. [56], varies with η over the range ±(0.5–1.5)%. For high E_{T}, the uncertainty in the photon energy resolution is dominated by the uncertainty in the constant term of the calorimetric energy resolution; at $E_{\mathrm{T}} = 300$ GeV, the relative uncertainty is ±(30–40)% depending on η. For jets with $100 < p_{\mathrm{T}} < 500$ GeV, the uncertainty in the jet energy scale is found to be less than ±1% [65]. Due to uncertainties in corrections for pileup, this uncertainty rises with falling p_{T}, reaching a value of about ±4.5% at $p_{\mathrm{T}} = 20$ GeV. Uncertainties in the values of whole-event observables, such as $E_{\mathrm{T}}^{\mathrm{miss}}$ and H_{T}, arise from uncertainties in the energy of the objects from which they are constructed. In addition, the $E_{\mathrm{T}}^{\mathrm{miss}}$ observable receives a contribution from tracks not associated with any of the reconstructed objects in the event [70]. Uncertainties arising from the inclusion of these unassigned contributions are found to contribute negligibly to the overall uncertainty in the value of the $E_{\mathrm{T}}^{\mathrm{miss}}$ observable.

In the regions of GGM parameter space relevant for establishing the exclusion limits discussed in Section 8, and excepting MC statistical uncertainty, the quadrature sum of the individual sources of systematic uncertainty in the signal reconstruction efficiency in the diphoton analysis is of order ±5%, and is dominated by the uncertainties in photon identification and the calorimetric energy scales. In the photon+jets analysis the systematic uncertainty is larger (approximately ±20%), due partially to an increased sensitivity to the jet-energy scale and resolution associated with the multiple-jet requirement.

9 Results

The number of events observed in each SR is shown in Table 8, along with the size of the expected SM background. These results are also illustrated in Figures 4 and 6, with the expected background broken down into its contributing SM sources. No significant evidence for physics beyond the SM is observed in any of the SRs.

The most significant excess relative to the expected background is observed for $\mathrm{SR}_{\mathrm{L200}}^{\gamma\mathrm{j}}$ of the photon+jets analysis. Considering both statistical and systematic uncertainty, and assuming that all observed events are from SM sources, an observation of eight or more events over an expected background of $2.68^{+0.64}_{-0.63}$ events represents an upward fluctuation with a probability of occurrence of approximately 0.9%.

Based on the numbers of observed and expected events in the seven SRs shown in Table 8, 95% CL upper limits are set for each SR on the number of events from any scenario of physics beyond the SM. These limits are based on the profile likelihood ratio [71] and $\mathrm{CL_s}$ [72] prescriptions, making use of the likelihood function described in Section 7. Assuming that no events due to physical processes beyond those of the SM populate the various CRs used to estimate SR backgrounds, observed 95% CL upper limits on the number of such events vary between 3.0 (for $\mathrm{SR}_{\mathrm{S-H}}^{\gamma\gamma}$ and $\mathrm{SR}_{\mathrm{S-L}}^{\gamma\gamma}$) and 11.5 (for $\mathrm{SR}_{\mathrm{L200}}^{\gamma\mathrm{j}}$). Taking into account the integrated luminosity of 36.1 fb^{-1} these number-of-event limits translate into 95% CL upper limits

Table 8: Summary of the observed number of events (N_{obs}), and the number of events expected from SM sources ($N_{\text{exp}}^{\text{SM}}$), for each of the seven SRs. Also shown are the derived (S_{obs}^{95}) and expected (S_{exp}^{95}) model-independent 95% CL limits on the number of events from non-SM processes, and the observed ($\langle\epsilon\sigma\rangle_{\text{obs}}^{95}$) and expected ($\langle\epsilon\sigma\rangle_{\text{exp}}^{95}$) 95% CL limits on the visible cross section from non-SM processes. The last column of the table shows the significance Z of the observed excess (if any), and the probability p, capped at 0.5, that a background-only experiment is more signal-like than the observed number of events in the given signal region.

Signal Region	N_{obs}	$N_{\text{exp}}^{\text{SM}}$	S_{obs}^{95}	S_{exp}^{95}	$\langle\epsilon\sigma\rangle_{\text{obs}}^{95}$[fb]	$\langle\epsilon\sigma\rangle_{\text{exp}}^{95}$[fb]	Z (p)
$\text{SR}_{\text{S-L}}^{\gamma\gamma}$	0	$0.50^{+0.30}_{-0.26}$	3.0	$3.1^{+1.4}_{-0.2}$	0.083	$0.086^{+0.039}_{-0.003}$	0.00 (0.50)
$\text{SR}_{\text{S-H}}^{\gamma\gamma}$	0	$0.48^{+0.30}_{-0.25}$	3.0	$3.1^{+1.3}_{-0.1}$	0.083	$0.086^{+0.036}_{-0.003}$	0.00 (0.50)
$\text{SR}_{\text{W-L}}^{\gamma\gamma}$	6	3.7 ± 1.1	8.6	$5.8^{+2.8}_{-1.6}$	0.238	$0.161^{+0.078}_{-0.044}$	1.06 (0.14)
$\text{SR}_{\text{W-H}}^{\gamma\gamma}$	1	$2.05^{+0.65}_{-0.63}$	3.7	$4.4^{+1.9}_{-1.0}$	0.103	$0.122^{+0.053}_{-0.028}$	0.00 (0.50)
$\text{SR}_{\text{L}}^{\gamma\text{j}}$	4	$1.33^{+0.54}_{-0.32}$	7.6	$4.7^{+1.6}_{-0.8}$	0.210	$0.130^{+0.044}_{-0.022}$	1.81 (0.035)
$\text{SR}_{\text{L200}}^{\gamma\text{j}}$	8	$2.68^{+0.64}_{-0.63}$	11.5	$5.4^{+2.2}_{-1.2}$	0.318	$0.151^{+0.060}_{-0.033}$	2.36 (0.009)
$\text{SR}_{\text{H}}^{\gamma\text{j}}$	3	$1.14^{+0.61}_{-0.36}$	6.6	$5.9^{+1.8}_{-1.1}$	0.183	$0.162^{+0.050}_{-0.030}$	1.20 (0.116)

on the visible cross section for new physics, defined as the product of cross section, branching fraction, acceptance and efficiency, for the different SR definitions. The resulting observed visible cross-section limits vary between 0.083 fb and 0.32 fb.

By considering, in addition to the event counts in the SRs, the values and uncertainties of the acceptance times efficiency of the SR selection requirements, as well as the NLO (+NLL) GGM cross sections [39–45], 95% CL lower limits are set on the masses of the accessible SUSY states of the GGM scenarios explored in this study. The SR with the best expected sensitivity at each simulated point in the parameter space of the corresponding GGM model(s) is used to determine the degree of exclusion of that model point.

For the diphoton analysis, in the region of gluino (squark) mass near the expected 95% CL exclusion limit, $\text{SR}_{\text{S-H}}^{\gamma\gamma}$ is expected to provide the greatest sensitivity to the gluino–bino (squark–bino) model for bino masses above 1600 GeV (900 GeV) and $\text{SR}_{\text{S-L}}^{\gamma\gamma}$ for bino masses below this value. For the wino–bino model, the similar transition point between the use of $\text{SR}_{\text{W-L}}^{\gamma\gamma}$ and $\text{SR}_{\text{W-H}}^{\gamma\gamma}$ is found to be at 400 GeV. The resulting observed limits on the gluino and wino masses are exhibited, as a function of bino mass, for the diphoton analysis gluino, squark and wino production models in Figures 8 through 10, respectively. For the purpose of establishing these model-dependent limits, both the normalization of the $W(\rightarrow \ell\nu) + \gamma\gamma$-background estimate and the limit on the possible number of events from new physics are extracted from a simultaneous fit to the SR and $W(\rightarrow \ell\nu) + \gamma\gamma$ control region. However, for masses near the various diphoton-analysis exclusion limits, the signal contamination in the $W(\rightarrow \ell\nu) + \gamma\gamma$ control sample is appreciable only for the wino–bino parameter space, reaching approximately 0.4 events (4% of the 9.1 events in the $\ell\gamma\gamma$ CR attributed to the $W(\rightarrow \ell\nu) + \gamma\gamma$ process) as the bino mass approaches zero. Also shown in these three figures, as well as in Figure 11, are the expected limits, including their statistical and background uncertainty ranges, as well as observed limits for SUSY model cross sections ±1 standard deviation of theoretical uncertainty from their central value. Considering all possible values of the $\tilde{\chi}_1^0$ mass, 95% CL lower limits of 2150 GeV, 1820 GeV and 1060 GeV are set by the diphoton analysis on

the value of the gluino, squark or wino mass, respectively, for any value of the NLSP bino mass less than that of the gluino, squark or wino mass. Based on a sample of 35.9 fb^{-1} of pp data accumulated at $\sqrt{s}$ = 13 TeV, and assuming a branching fraction of 100% for the photonic decay of the $\tilde{\chi}_1^0$, the CMS Collaboration has set 95% lower CL limits of 1790 GeV and 1580 GeV for similar models of gluino and squark production and decay, respectively [4]. For a GGM model similar to the wino–bino model of the diphoton analysis, a separate CMS Collaboration analysis [4] has set a 95% lower CL limit as high as 1000 GeV on the wino mass, depending on the value of the bino-like $\tilde{\chi}_1^0$ mass.

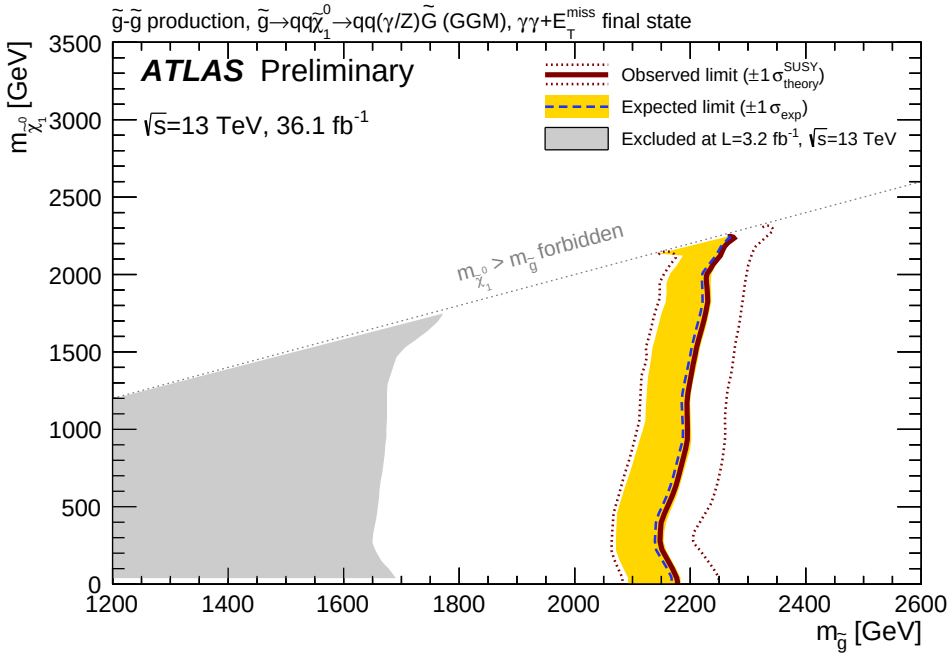

Figure 8: Exclusion limits in the gluino–bino mass plane, using the $\mathrm{SR}_{\mathrm{S-H}}^{\gamma\gamma}$ analysis for $m_{\tilde{\chi}_1^0} > 1600$ GeV and the $\mathrm{SR}_{\mathrm{S-L}}^{\gamma\gamma}$ analysis for $m_{\tilde{\chi}_1^0} < 1600$ GeV. Combinations of gluino and bino mass are excluded at greater than 95% CL in the area to the left of the unbroken curve. The observed limits are exhibited for the nominal SUSY model cross-section expectation, as well as for a SUSY cross section increased and decreased by 1 standard deviation of the cross-section systematic uncertainty. Also shown is the expected limit, as well as the ±1 standard-deviation range of the expected limit, which is asymmetric due to the small number of expected events. The gray region is that previously excluded with the 2015 data sample; see Ref. [3].

Using the photon+jets analysis, limits are set in the two-dimensional plane of the masses of the gluino and the mixed higgsino–bino NLSP. For values of $m_{\tilde{g}}$ and $m_{\tilde{\chi}_1^0}$ close to the expected 95% CL exclusion limit, $\mathrm{SR}_{\mathrm{L}}^{\gamma\mathrm{j}}$ is expected to provide a greater sensitivity for NLSP masses below approximately 1500 GeV, and so is made use of in this region; for higher NLSP masses, $\mathrm{SR}_{\mathrm{H}}^{\gamma\mathrm{j}}$ is used to establish the degree of exclusion of points in the GGM-model parameter space. The resulting observed exclusion contour is shown in Figure 11. In the context of this GGM model, lower limits as high as 2050 GeV are established for the gluino mass, depending on the value of $m_{\tilde{\chi}_1^0}$. The sensitivity of the analysis has not been explored for values of the NLSP mass within 50 GeV of that of the gluino, where the selection efficiency diminishes due to the restriction of phase space for producing multiple high-p_{T} jets, and the tendency of the gluino to become metastable as the splitting between the gluino and $\tilde{\chi}_1^0$ mass becomes small.

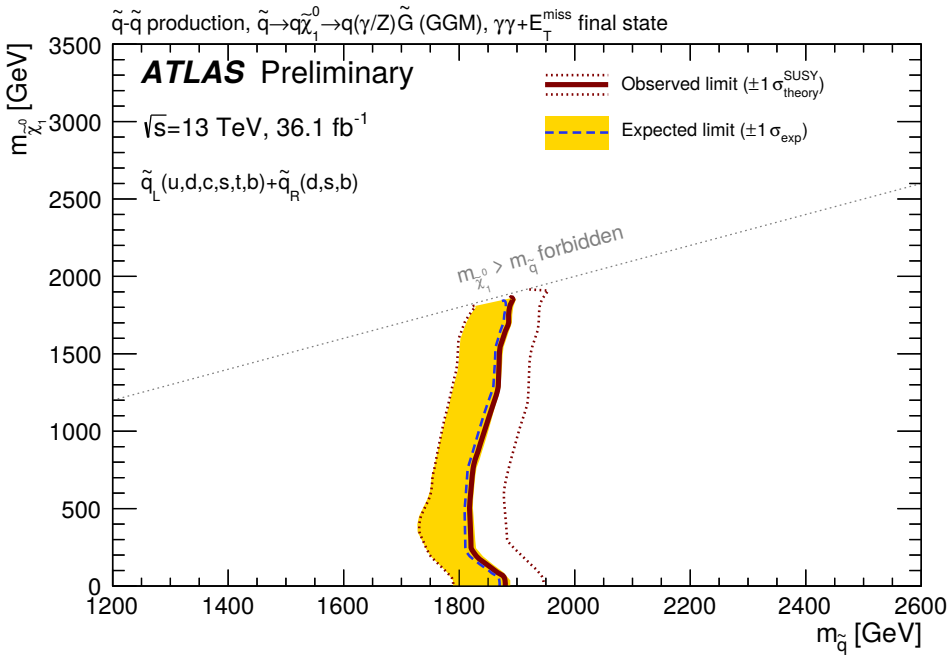

Figure 9: Exclusion limits in the squark–bino mass plane, using the $\mathrm{SR}^{\gamma\gamma}_{\mathrm{S-H}}$ analysis for $m_{\tilde{\chi}^0_1} > 900$ GeV and the $\mathrm{SR}^{\gamma\gamma}_{\mathrm{S-L}}$ analysis for $m_{\tilde{\chi}^0_1} < 900$ GeV. Combinations of squark and bino mass are excluded at greater than 95% CL in the area to the left of the unbroken curve. The observed limits are exhibited for the nominal SUSY model cross-section expectation, as well as for a SUSY cross section increased and decreased by 1 standard deviation of the cross-section systematic uncertainty. Also shown is the expected limit, as well as the ±1 standard-deviation range of the expected limit, which is asymmetric due to the small number of expected events.

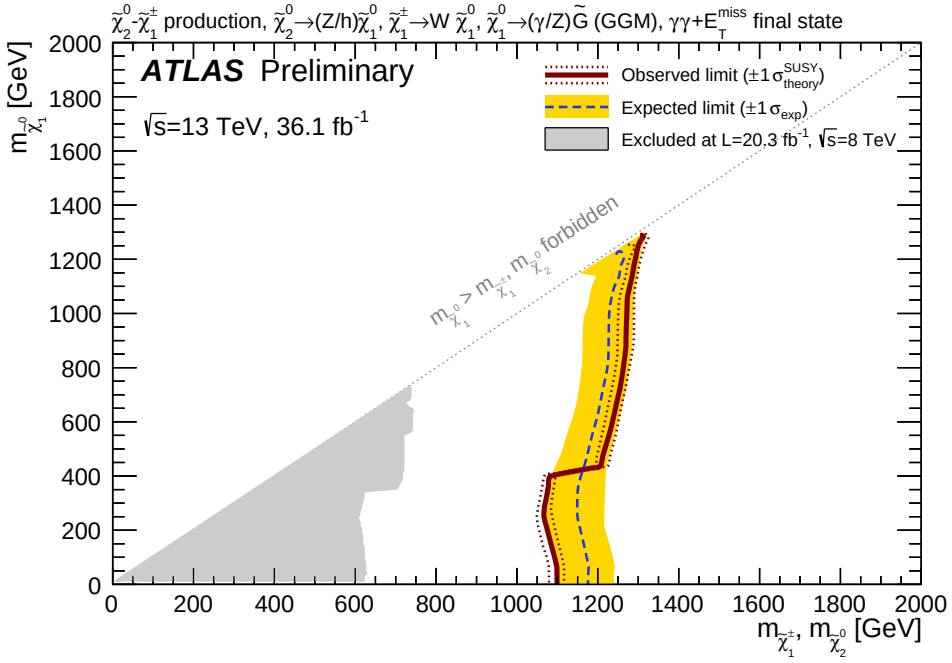

Figure 10: Exclusion limits in the wino–bino mass plane, using the $\mathrm{SR}^{\gamma\gamma}_{\mathrm{W-H}}$ analysis for $m_{\tilde{\chi}_1^0} > 400$ GeV and the $\mathrm{SR}^{\gamma\gamma}_{\mathrm{W-L}}$ analysis for $m_{\tilde{\chi}_1^0} < 400$ GeV. The vertical axis represents bino mass while the horizontal axis represents wino mass. Combinations of wino and bino mass are excluded at greater than 95% CL in the area to the left of the unbroken curve. The observed limits are exhibited for the nominal SUSY model cross-section expectation, as well as for a SUSY cross section increased and decreased by 1 standard deviation of the cross-section systematic uncertainty. Also shown is the expected limit, along with its ±1 standard-deviation range. The discontinuity at $m_{\tilde{\chi}_1^0} = 400$ GeV is due to the switch between the use of the $\mathrm{SR}^{\gamma\gamma}_{\mathrm{W-L}}$ and $\mathrm{SR}^{\gamma\gamma}_{\mathrm{W-H}}$ analyses, the former of which exhibits a small excess of observed events relative to the expected SM background. The gray region is that previously excluded with the data sample taken at $\sqrt{s} = 8$ TeV; see Ref. [6].

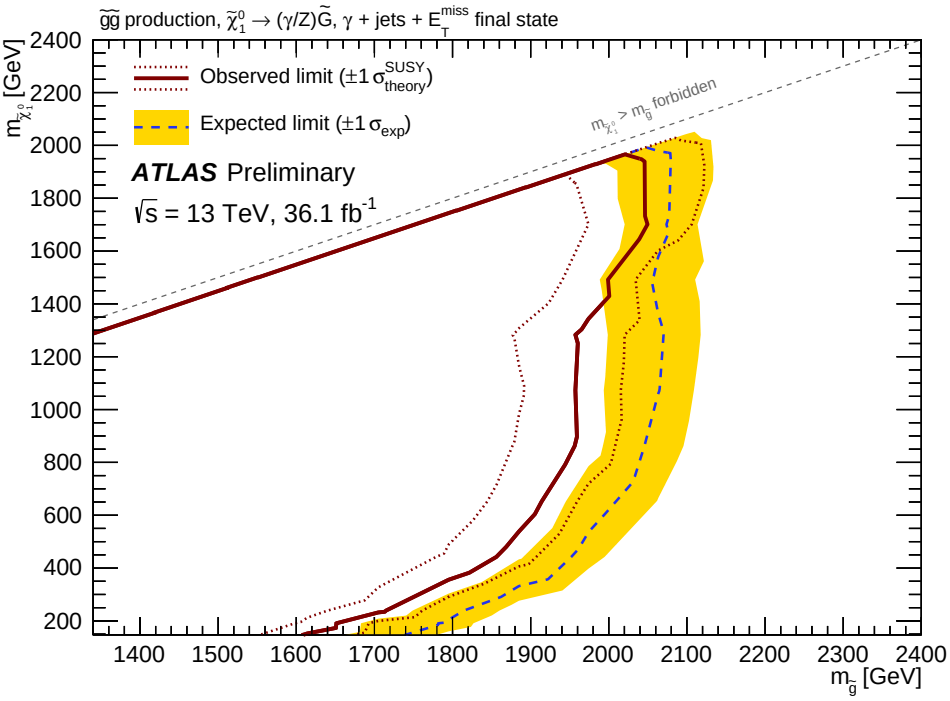

Figure 11: Derived exclusion limits for the $\mu > 0$ higgsino–bino GGM model explored by the photon+jets analysis. For this figure, the underlying model parameters M_3 and μ have been transformed to the physical parameters $m_{\tilde{g}}$ and $m_{\tilde{\chi}_1^0}$, under the assumptions stated in Section 2. For each point in the higgsino–bino parameter space, the SR ($SR_L^{\gamma j}$ or $SR_H^{\gamma j}$) that provides the best expected sensitivity is used to estimate the exclusion likelihood. Combinations of gluino and neutralino mass are excluded at greater than 95% CL in the area to the left of the unbroken curve. The observed limits are shown for the nominal SUSY model cross-section expectation, as well as for a SUSY cross section increased and decreased by 1 standard deviation of the cross-section systematic uncertainty. The expected limit is also shown, along with its ± 1 standard-deviation range.

10 Conclusion

Making use of proton–proton collision data at $\sqrt{s} = 13$ TeV corresponding to an integrated luminosity of 36.1 fb^{-1} recorded by the ATLAS detector at the LHC in 2015 and 2016, a search is performed for photonic signatures of new physics associated with significant missing transverse momentum. Both single-photon and diphoton selection strategies were developed and used to search for evidence for several general gauge-mediated (GGM) SUSY-breaking scenarios. No significant excess of events over the Standard Model expectation is observed in any of the searches and limits are set on possible contributions of new physics. Model-independent limits between 0.083 fb and 0.32 fb are set on the associated visible cross section of contributions from physics beyond the Standard Model.

Based on these limits on contributions from new physics, model-dependent limits are set on the masses of SUSY particles within the context of GGM. A diphoton signature is used to explore both strongly and weakly produced SUSY states with a decay chain proceeding through a bino-like next-to-lightest supersymmetric particle (NLSP). In the context of these models, lower limits of 2150 GeV, 1820 GeV and 1060 GeV are set on the masses of gluinos, squarks and a degenerate set of winos, respectively, for any value of the bino mass less than the mass of these produced states. In addition, a photon+jets signature is used to search for an alternative scenario for which the GGM NLSP is a higgsino–bino admixture with a roughly equal branching fraction to photons and to the Z boson. In the context of this model, lower limits as high as 2050 GeV are established for the gluino mass, depending on the value of the NLSP mass.

References

[1] C. Cheung, A. L. Fitzpatrick, and D. Shih, *(Extra)ordinary gauge mediation*, JHEP **0807** (2008) p. 054, arXiv: 0710.3585 [hep-ph].

[2] P. Meade, N. Seiberg, and D. Shih, *General Gauge Mediation*, Prog. Theor. Phys. Suppl. **177** (2009) p. 143, arXiv: 0801.3278 [hep-ph].

[3] ATLAS Collaboration, *Search for supersymmetry in a final state containing two photons and missing transverse momentum in* $\sqrt{s} = 13$ *TeV pp collisions at the LHC using the ATLAS detector*, Eur. Phys. J. C **76** (2016) p. 517, arXiv: 1606.09150 [hep-ex].

[4] CMS Collaboration, *Search for supersymmetry in events with at least one photon, missing transverse momentum, and large transverse event activity in proton-proton collisions at* $\sqrt{s} = 13$ *TeV*, (2017), arXiv: 1707.06193 [hep-ex].

[5] CMS Collaboration, *Search for gauge-mediated supersymmetry in events with at least one photon and missing transverse momentum in pp collisions at* $\sqrt{s} = 13$ *TeV*, (2017), arXiv: 1711.08008 [hep-ex].

[6] ATLAS Collaboration, *Search for photonic signatures of gauge-mediated supersymmetry in* 8 *TeV pp collisions with the ATLAS detector*, Phys. Rev. D **92** (2015) p. 072001, arXiv: 1507.05493 [hep-ex].

[7] Y. A. Gol'fand and E. P. Likhtman, *Extension of the Algebra of Poincare Group Generators and Violation of p Invariance*, JETP Lett. **13** (1971) p. 323, [Pisma Zh.Eksp.Teor.Fiz. 13:452-455,1971].

[8] D. V. Volkov and V. P. Akulov, *Is the Neutrino a Goldstone Particle?*, Phys. Lett. B **46** (1973) p. 109.

[9] J. Wess and B. Zumino, *Supergauge Transformations in Four-Dimensions*, Nucl. Phys. B **70** (1974) p. 39.

[10] J. Wess and B. Zumino, *Supergauge Invariant Extension of Quantum Electrodynamics*, Nucl. Phys. B **78** (1974) p. 1.

[11] S. Ferrara and B. Zumino, *Supergauge Invariant Yang-Mills Theories*, Nucl. Phys. B **79** (1974) p. 413.

[12] A. Salam and J. A. Strathdee, *Supersymmetry and Nonabelian Gauges*, Phys. Lett. B **51** (1974) p. 353.

[13] S. P. Martin, *A Supersymmetry primer. Perspectives on Supersymmetry*, Adv. Set. Direct. High Energy Physics **18** (1998) p. 1, arXiv: hep-ph/9709356.

[14] S. P. Martin, *A Supersymmetry primer. Perspectives on Supersymmetry II*, Adv. Set. Direct. High Energy Physics **21** (2010) p. 1, arXiv: hep-ph/9709356.

[15] P. Fayet, *Supersymmetry and Weak, Electromagnetic and Strong Interactions*, Phys. Lett. B **64** (1976) p. 159.

[16] P. Fayet, *Spontaneously Broken Supersymmetric Theories of Weak, Electromagnetic and Strong Interactions*, Phys. Lett. B **69** (1977) p. 489.

[17] G. R. Farrar and P. Fayet, *Phenomenology of the Production, Decay, and Detection of New Hadronic States Associated with Supersymmetry*, Phys. Lett. B **76** (1978) p. 575.

[18] P. Fayet, *Relations Between the Masses of the Superpartners of Leptons and Quarks, the Goldstino Couplings and the Neutral Currents*, Phys. Lett. B **84** (1979) p. 416.

[19] S. Dimopoulos and H. Georgi, *Softly Broken Supersymmetry and SU(5)*, Nucl. Phys. B **193** (1981) p. 150.

[20] M. Dine and W. Fischler, *A Phenomenological Model of Particle Physics Based on Supersymmetry*, Phys. Lett. B **110** (1982) p. 227.

[21] L. Alvarez-Gaume, M. Claudson, and M. B. Wise, *Low-Energy Supersymmetry*, Nucl. Phys. B **207** (1982) p. 96.

[22] C. R. Nappi and B. A. Ovrut, *Supersymmetric Extension of the SU(3) x SU(2) x U(1) Model*, Phys. Lett. B **113** (1982) p. 175.

[23] M. Dine and A. E. Nelson, *Dynamical supersymmetry breaking at low-energies*, Phys. Rev. **48** (1993) p. 1277, arXiv: hep-ph/9303230.

[24] M. Dine, A. E. Nelson, and Y. Shirman, *Low-energy dynamical supersymmetry breaking simplified*, Phys. Rev. D **51** (1995) p. 1362, arXiv: hep-ph/9408384.

[25] M. Dine, A. E. Nelson, Y. Nir, and Y. Shirman, *New tools for low-energy dynamical supersymmetry breaking*, Phys. Rev. D **53** (1996) p. 2658, arXiv: hep-ph/9507378.

[26] ATLAS Collaboration, *Search for nonpointing and delayed photons in the diphoton and missing transverse momentum final state in 8 TeV pp collisions at the LHC using the ATLAS detector*, Phys. Rev. D **90** (2014) p. 112005, arXiv: 1409.5542 [hep-ex].

[27] ATLAS Collaboration, *The ATLAS Experiment at the CERN Large Hadron Collider*, JINST **3** (2008) S08003.

[28] ATLAS Collaboration, *ATLAS Insertable B-Layer Technical Design Report*, ATLAS-TDR-19, 2010, URL: https://cds.cern.ch/record/1291633, ATLAS Insertable B-Layer Technical Design Report Addendum, ATLAS-TDR-19-ADD-1, 2012, URL: https://cds.cern.ch/record/1451888.

[29] ATLAS Collaboration, *Performance of the ATLAS trigger system in 2015*, Eur. Phys. J. C **77** (2017) p. 317, arXiv: 1611.09661 [hep-ex].

[30] A. Djouadi, J.-L. Kneur, and G. Moultaka, *SuSpect: A Fortran code for the supersymmetric and Higgs particle spectrum in the MSSM*, Comput. Phys. Commun. **176** (2007) p. 426, arXiv: hep-ph/0211331.

[31] M. Muhlleitner, *SDECAY — a Fortran Code for the Calculation of Supersymmetric Particle Decays*, Acta Phys. Polon. B **35** (2004) p. 2753, arXiv: hep-ph/0409200.

[32] A. Djouadi, M. Muhlleitner, and M. Spira, *Decays of supersymmetric particles: The Program SUSY-HIT (SUspect-SdecaY-Hdecay-InTerface)*, Acta Phys. Polon. B **38** (2007) p. 635, arXiv: hep-ph/0609292.

[33] A. Djouadi, J. Kalinowski, and M. Spira, *HDECAY: a program for Higgs boson decays in the Standard Model and its supersymmetric extension*, Comput. Phys. Commun. **108** (1998) p. 56, arXiv: hep-ph/9704448.

[34] M. Mühlleitner, A. Djouadi, and Y. Mambrini,
SDECAY: A Fortran code for the decays of the supersymmetric particles in the MSSM,
Comput. Phys. Commun. **168** (2005) p. 46, arXiv: hep-ph/0311167.

[35] J. Alwall et al., *The automated computation of tree-level and next-to-leading order differential cross sections, and their matching to parton shower simulations*, JHEP **1407** (2014) p. 079,
arXiv: 1405.0301 [hep-ph].

[36] R. D. Ball et al., *Parton distributions with LHC data*, Nucl. Phys. B **867** (2013) p. 244,
arXiv: 1207.1303 [hep-ph].

[37] T. Sjöstrand et al., *An introduction to PYTHIA 8.2*, Comput. Phys. Commun. **191** (2015) p. 159,
arXiv: 1410.3012 [hep-ph].

[38] ATLAS Collaboration, *ATLAS Pythia 8 tunes to 7 TeV data*, ATL-PHYS-PUB-2014-021, 2014,
URL: https://cds.cern.ch/record/1966419.

[39] W. Beenakker, R. Höpker, M. Spira, and P. M. Zerwas,
Squark and gluino production at hadron colliders, Nucl. Phys. B **492** (1997) p. 51,
arXiv: hep-ph/9610490.

[40] A. Kulesza and L. Motyka,
Threshold resummation for squark-antisquark and gluino- pair production at the LHC,
Phys. Rev. Lett. **102** (2009) p. 111802, arXiv: 0807.2405 [hep-ph].

[41] A. Kulesza and L. Motyka, *Soft gluon resummation for the production of gluino-gluino and squark-antisquark pairs at the LHC*, Phys. Rev. D **80** (2009) p. 095004,
arXiv: 0905.4749 [hep-ph].

[42] W. Beenakker et al., *Soft-gluon resummation for squark and gluino hadroproduction*,
JHEP **0912** (2009) p. 041, arXiv: 0909.4418 [hep-ph].

[43] W. Beenakker et al., *Squark and gluino hadroproduction*, Int. J. Mod. Phys. A **26** (2011) p. 2637,
arXiv: 1105.1110 [hep-ph].

[44] B. Fuks, M. Klasen, D. R. Lamprea, and M. Rothering,
Gaugino production in proton-proton collisions at a center-of-mass energy of 8 TeV,
JHEP **1210** (2012) p. 081, arXiv: 1207.2159 [hep-ph].

[45] B. Fuks, M. Klasen, D. R. Lamprea, and M. Rothering, *Precision predictions for electroweak superpartner production at hadron colliders with Resummino*, Eur. Phys. J. C **73** (2013) p. 2480,
arXiv: 1304.0790 [hep-ph].

[46] C. Borschensky et al.,
Squark and gluino production cross sections in pp collisions at $\sqrt{s}$ = 13, 14, 33 and 100 TeV,
Eur. Phys. J. C **74** (2014) p. 3174, arXiv: 1407.5066 [hep-ph].

[47] T. Gleisberg et al., *Event generation with SHERPA 1.1*, JHEP **0902** (2009) p. 007,
arXiv: 0811.4622 [hep-ph].

[48] H.-L. Lai et al., *New parton distributions for collider physics*, Phys. Rev. D **82** (2010) p. 074024,
arXiv: 1007.2241 [hep-ph].

[49] T. Gleisberg and S. Hoeche, *Comix, a new matrix element generator*, JHEP **0812** (2008) p. 039,
arXiv: 0808.3674 [hep-ph].

[50] S. Schumann and F. Krauss,
A Parton shower algorithm based on Catani-Seymour dipole factorisation,
JHEP **0803** (2008) p. 038, arXiv: 0709.1027 [hep-ph].

[51] S. Hoeche, F. Krauss, S. Schumann, and F. Siegert, *QCD matrix elements and truncated showers*,
JHEP **0905** (2009) p. 053, arXiv: 0903.1219 [hep-ph].

[52] T. Sjöstrand, S. Mrenna, and P. Z. Skands, *A brief introduction to PYTHIA 8.1*,
Comput. Phys. Commun. **178** (2008) p. 852, arXiv: 0710.3820 [hep-ph].

[53] ATLAS Collaboration, *The ATLAS Simulation Infrastructure*, Eur. Phys. J. C **70** (2010) p. 823,
arXiv: 1005.4568 [physics.ins-det].

[54] S. Agostinelli et al., *GEANT4: A simulation toolkit*, Nucl. Instrum. Meth. A **506** (2003) p. 250.

[55] ATLAS Collaboration, *Electron efficiency measurements with the ATLAS detector using 2012 LHC proton–proton collision data*, Eur. Phys. J. C **77** (2017) p. 195,
arXiv: 1612.01456 [hep-ex].

[56] ATLAS Collaboration,
Electron and photon energy calibration with the ATLAS detector using LHC Run 1 data,
Eur. Phys. J. C **74** (2014) p. 3071, arXiv: 1407.5063 [hep-ex].

[57] ATLAS Collaboration, *Electron efficiency measurements with the ATLAS detector using the 2015 LHC proton–proton collision data*, ATLAS-CONF-2016-024, 2016,
URL: https://cds.cern.ch/record/2157687.

[58] ATLAS Collaboration, *Expected photon performance in the ATLAS experiment*,
ATL-PHYS-PUB-2011-007, 2011, URL: https://cds.cern.ch/record/1345329.

[59] ATLAS Collaboration, *Measurement of the photon identification efficiencies with the ATLAS detector using LHC Run-1 data*, Eur. Phys. J. C **76** (2016) p. 666, arXiv: 1606.01813 [hep-ex].

[60] ATLAS Collaboration, *Muon reconstruction performance of the ATLAS detector in proton–proton collision data at* $\sqrt{s} = 13$ *TeV*, Eur. Phys. J. C **76** (2016) p. 292, arXiv: 1603.05598 [hep-ex].

[61] M. Cacciari and G. P. Salam and G. Soyez, *FastJet user manual*, Eur. Phys. J. C **72** (2012) p. 1896,
arXiv: 1111.6097 [hep-ph].

[62] ATLAS Collaboration,
Topological cell clustering in the ATLAS calorimeters and its performance in LHC Run 1,
Eur. Phys. J. C **77** (2017) p. 490, arXiv: 1603.02934 [hep-ex].

[63] M. Cacciari, G. P. Salam, and G. Soyez, *The anti-*k_t *jet clustering algorithm*,
JHEP **0804** (2008) p. 063, arXiv: 0802.1189 [hep-ph].

[64] ATLAS Collaboration,
A measurement of the calorimeter response to single hadrons and determination of the jet energy scale uncertainty using LHC Run-1 pp-collision data with the ATLAS detector,
Eur. Phys. J. C **77** (2017) p. 26, arXiv: 1607.08842 [hep-ex].

[65] ATLAS Collaboration, *Jet energy scale measurements and their systematic uncertainties in proton–proton collisions at* $\sqrt{s} = 13$ *TeV with the ATLAS detector*,
Phys. Rev. D **96** (2017) p. 072002, arXiv: 1703.09665 [hep-ex].

[66] ATLAS Collaboration, *Optimisation of the ATLAS b-tagging performance for the 2016 LHC Run*,
ATL-PHYS-PUB-2016-012, 2016, URL: https://cds.cern.ch/record/2160731.

[67] ATLAS Collaboration, *Performance of b-Jet Identification in the ATLAS Experiment*, JINST **11** (2016) P04008, arXiv: 1512.01094 [hep-ex].

[68] G. Bozzi, F. Campanario, M. Rauch, and D. Zeppenfeld, *$W\gamma\gamma$ production with leptonic decays at NLO QCD*, Phys. Rev. D **83** (2011) p. 114035, arXiv: 1103.4613 [hep-ph].

[69] ATLAS Collaboration, *Luminosity determination in pp collisions at $\sqrt{s} = 8$ TeV using the ATLAS detector at the LHC*, Eur. Phys. J. C **76** (2016) p. 653, arXiv: 1608.03953 [hep-ex].

[70] ATLAS Collaboration, *Performance of algorithms that reconstruct missing transverse momentum in $\sqrt{s} = 8$ TeV proton–proton collisions in the ATLAS detector*, Eur. Phys. J. C **77** (2017) p. 241, arXiv: 1609.09324 [hep-ex].

[71] M. Baak et al., *HistFitter software framework for statistical data analysis*, Eur. Phys. J. C **75** (2015) p. 153, arXiv: 1410.1280 [hep-ex].

[72] A. L. Read, *Presentation of search results: The CL_s technique*, J. Phys. G **28** (2002) p. 2693.